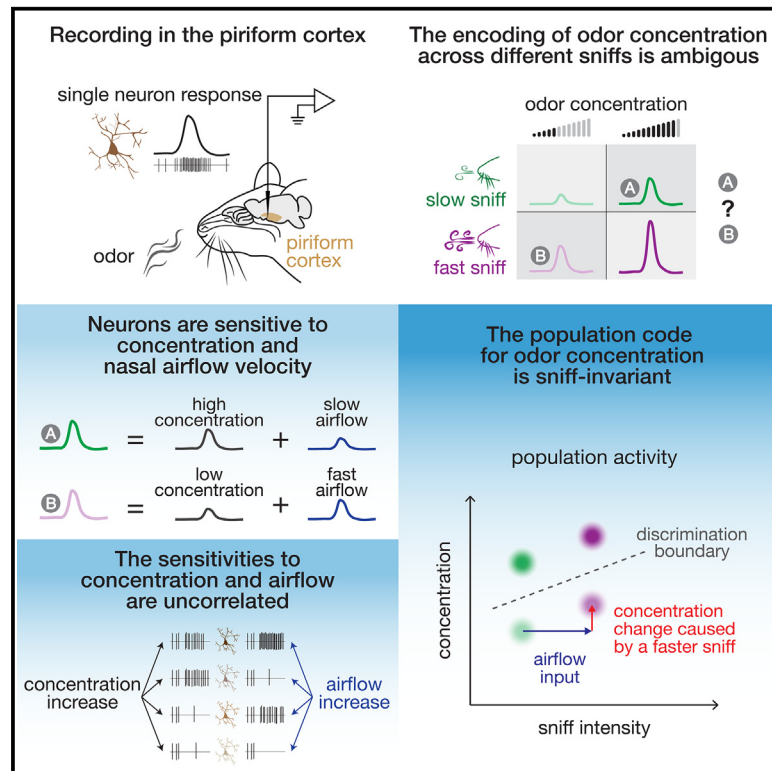# A mechanosensory feedback that uncouples external and self-generated sensory responses in the olfactory cortex

Graphical abstract

Authors

Alireza A. Dehaqani, Filippo Michelon, Paola Patella, Luigi Petrucco, Eugenio Piasini, Giuliano Iurilli

Correspondence

giuliano.iurilli@iit.it

In brief

Dehaqani et al. reveal that inhalation speed affects the olfactory responses of individual neurons, challenging stable odor concentration representation. However, odor and inhalation information in the olfactory cortex remain independent at the population level. Thus, the cortical representation of concentration is robust to the sensory consequences of sniffing.

Highlights

- Sniffing affects odor responses in the main olfactory cortex

- Cortical neurons encode the nasal airflow velocity

- Cortical neurons combine odor and airflow information additively

- The population code for odor concentration remains sniff invariant

CellPress

Article

A mechanosensory feedback that uncouples external and self-generated sensory responses in the olfactory cortex

Alireza A. Dehaqani,[1,2,4] Filippo Michelon,[1,2,4] Paola Patella,[1] Luigi Petrucco,[1] Eugenio Piasini,[3] and Giuliano Iurilli[1,5,*]

[1]Center for Neuroscience and Cognitive Systems, Istituto Italiano di Tecnologia, 38068 Rovereto, Italy
[2]CIMeC, University of Trento, 38068 Rovereto, Italy
[3]International School for Advanced Studies (SISSA), Trieste, Italy
[4]These authors contributed equally
[5]Lead contact
*Correspondence: giuliano.iurilli@iit.it
https://doi.org/10.1016/j.celrep.2024.114013

SUMMARY

Sampling behaviors have sensory consequences that can hinder perceptual stability. In olfaction, sniffing affects early odor encoding, mimicking a sudden change in odor concentration. We examined how the inhalation speed affects the representation of odor concentration in the main olfactory cortex. Neurons combine the odor input with a global top-down signal preceding the sniff and a mechanosensory feedback generated by the air passage through the nose during inhalation. Still, the population representation of concentration is remarkably sniff invariant. This is because the mechanosensory and olfactory responses are uncorrelated within and across neurons. Thus, faster odor inhalation and an increase in concentration change the cortical activity pattern in distinct ways. This encoding strategy affords tolerance to potential concentration fluctuations caused by varying inhalation speeds. Since mechanosensory reafferences are widespread across sensory systems, the coding scheme described here may be a canonical strategy to mitigate the sensory ambiguities caused by movements.

INTRODUCTION

A problem animals face as they explore the world is that their own actions generate sensory stimuli that can be indistinguishable from those caused by external events. A consequence of this ambiguity is that stimulus encoding becomes subject to the moment-by-moment variability of sampling movements.[1] In olfaction, this problem arises whenever an animal changes how fast it samples an odorant.[2–5] In terrestrial vertebrates, breathing through the nose provides the animal with repeated snapshots of the olfactory world.[6] Animals can compare these sequential samples to analyze the olfactory scene, detecting changes in odors and their concentration.[7–9] However, when an animal takes rapid breaths, the nasal airflow rate increases. As a result, the concentration profile of an odor inside the nasal cavity is thought to change, mimicking an increase in the environmental odor concentration.[2–4]

Odorants are detected by receptors expressed by the olfactory sensory neurons (OSNs). OSNs innervate the main olfactory bulbs (OBs), which transform olfactory information and broadcast their output to higher brain centers through projection neurons called mitral/tufted (MT) neurons. Consistent with the effect of the nasal airflow on the number of molecules that reach the olfactory epithelium, sniffing alters odor responses at the early stages of olfactory processing.[10–12] Remarkably, faster sniffs in-

crease the magnitude and reduce the latency of the odor responses of the MT neurons as if the external concentration had suddenly increased.[4,5] Nevertheless, humans and rodents can quickly learn to distinguish the concentration of odors regardless of the inhalation speed.[2,4,5] How these physiological and behavioral results can be reconciled is a long-standing question.

It has been proposed that an animal can discriminate an increase in the environmental concentration from the effect of a faster inhalation because the olfactory system may encode how fast the animal is breathing.[2–5] This hypothesis is supported by the observation that nasal breathing entrains the activity of the olfactory system even in the absence of odors[11,13–19]; moreover, it has been demonstrated that the spiking activity of MT neurons encodes the duration of an inhalation.[5] Still, the origin and content of this information are unclear. Efferent copies of the inhalation command could predict the airflow kinematics in the nasal cavities; however, there is currently no evidence of motor inputs to the olfactory system. Instead, since many olfactory receptors respond to mechanical stimuli as well as to odorants,[20,21] the information about the inhalation speed could be supplied by the air passing through the nose during each inhalation. Notably, however, this latter possibility also highlights another potential problem arising with each inhalation. Because mechanosensory and olfactory inputs have the same source, the airflow signal could
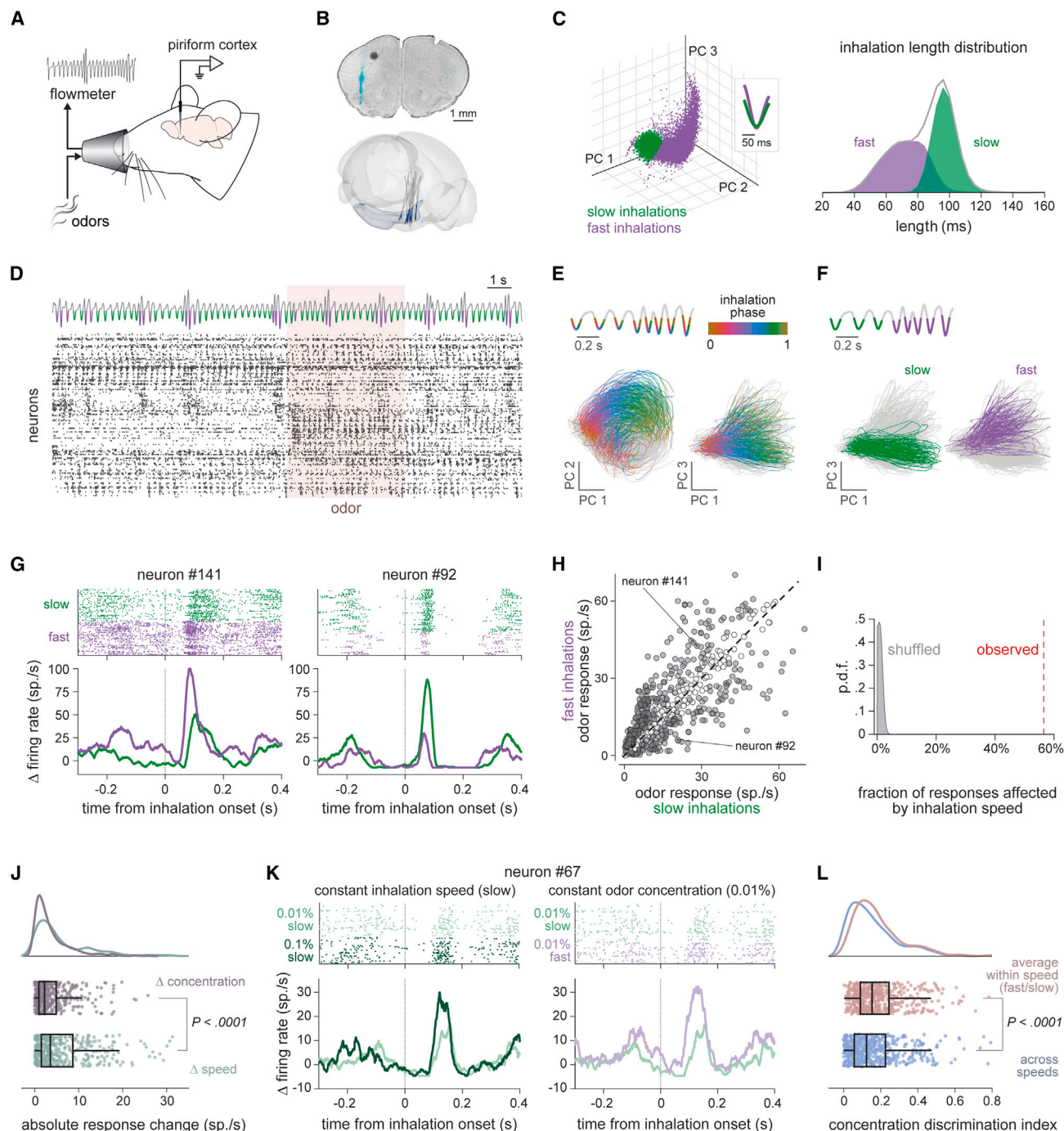
Figure 1. Sniffing causes unstable odor responses in the PCx

(A) Experimental setup for PCx recordings paired with odor delivering and inhalation monitoring.

(B) Recording sites. Top, example of coronal section indicating the placement of a Neuropixels probe in the anterior PCx (cyan). Bottom, reconstructed locations of Neuropixels probes from all experiments (n = 22 mice). Scale bar: 1 mm.

(C) Types of inhalations. Left, PCA plot of inhalation waveforms sorted via Gaussian-mixture model-hierarchical clustering; inset, average slow (green) and fast (purple) inhalation waveforms. Right, distribution of slow and fast inhalation lengths. Gray curve, length distribution before inhalation sorting.

(D) Example of simultaneous PCx activity and respiratory airflow rate. External flow sensor signal (top) and spiking raster plot (bottom). Shaded area, odor period (5 s). Slow and fast inhalations are color coded in green and purple, respectively.

(E) PCA embedding of neural trajectories during individual respiratory cycles for an example mouse (time bin: 10 ms). The inhalation phase is color coded according to the scheme in the inset plot on the top (inhalation onset, 0; offset, 1). Gray, exhalation.

(legend continued on next page)

actually increase confusion and interfere with olfactory information, further hindering the representation of odor concentration. Thus, whether and how a non-olfactory signal could help distinguish the olfactory consequences of sniffing remain to be determined.

Here, we set out to examine whether the speed of inhalation affects the representation of odor concentration in a higher-order area called the piriform cortex (PCx). The PCx represents odors through a population code, in which the distributed activity of ensembles of neurons affords downstream brain areas systematic information about odor identity and concentration.[22–28] Recording the spiking activity of ensembles of neurons, we observed that odor responses are primarily sensitive to the mechanical stimulation of the olfactory epithelium by inhaled air and to a global top-down input that seems to precede sniffs. The mechanosensory response to a quick breath can increase or decrease relative to a regular inhalation, independent of how the neuron responds to a concentration increase. As a result, the mechanosensory response distinguishes the population representation of an odor during a sniff without interfering with the representation of the concentration of that odor, effectively ensuring a sniff-invariant concentration code.

RESULTS

Sniffing causes unstable odor responses in the PCx

To determine the effects of inhalation speed on odor responses in the PCx, we used Neuropixels 1.0 probes to record inhalation-by-inhalation responses to different odor concentrations in awake, head-fixed mice (Figures 1A and 1B). We monitored inhalations through a flow sensor in front of the mouse naris. The flow sensor measured the airflow rate at the entrance of the nasal cavity during each inhalation. Since the distribution of inhalation durations appeared bimodal, we developed a semi-unsupervised method that sorted inhalations into slow and fast depending on their airflow rate waveforms (Figure 1C; see STAR Methods). Fast inhalations had shorter duration and steeper changes in airflow rate than slow inhalations. We use "sniff" and "fast inhalation" interchangeably, regardless of whether the origin was autonomic or volitional.[29]

Our neural recordings sampled excitatory (semilunar and pyramidal) and inhibitory neurons from layers 2 and 3 of the anterior PCx. We used two spike waveform features, i.e., asymmetry and through-to-peak delay, as surrogate indicators for the different neuron types in the PCx. The distributions of the waveform features were comparable across experiments, and neither cross-validated linear nor non-linear classifiers could discriminate an experimental condition based on the spike waveforms of the units recorded (see STAR Methods). These results suggest a homogenous sampling of neural cell types across experimental conditions.

Inhalations periodically activated most PCx neurons sequentially, and faster sniffs appeared to enhance the activity of some neurons while decreasing that of others (Figure 1D). Hence, PCx activity encoded the phase and speed of each inhalation (Figures 1E and 1F; Figures S1A and S1B). Of the recorded neurons, 31.1% reliably responded to at least one odor concentration (205 of 660 neurons; six mice). Strikingly, how fast an animal inhaled influenced the response amplitude during inhalation in 72.2% of those neurons (148 of 205 neurons; Figures 1G–1I). This proportion was a lower-bound estimate based on the responses to a panel of only five odors and two concentrations. The impact of a faster inhalation was not uniform across odor responses: 37.3% of the odor responses increased with a rapid inhalation, whereas 19.2% decreased in amplitude. This sniff-driven variability in odor responses was already significant during the first 70 ms of an inhalation (Figure S1C). Because GABAergic neurons providing feedback inhibition tend to exhibit narrower action potentials and faster activity,[23] we used these features to tentatively distinguish them from the other excitatory and feedforward inhibitory neurons. After sorting neurons into regular spiking (RS; putatively excitatory or feedforward inhibitory) and fast spiking (FS; putatively feedback inhibitory), we observed similar effects of the inhalation speed in both types (Figure S1D).

On average, sniffs caused a response amplitude change bigger than that caused by a 10-fold increase in odor concentration in the odor-responsive neurons (Figure 1J). Thus, changing the inhalation speed generated a large amount of response variability that could impair the discriminability of odor

---

(F) Same neural trajectories as in (E), color coded according to the inhalation speed. Green, slow inhalations; purple, fast inhalations.

(G) Examples of odor responses during slow and fast inhalations. Raster plot (top) and PETH (bottom) for two neurons from the same mouse responding to the same odor and concentration.

(H) Scatterplot of odor-response amplitudes (average firing rate in 180 ms window and across slow or fast inhalations; five odors, 0.01% and 0.1% v/v concentration; n = 750 odor-concentration responses) for all odor-responsive neurons (Benjamini-Hochberg adjusted p < 0.05, Wilcoxon signed-rank test; n = 205 neurons, 6 mice). Gray dots, significant difference between the amplitudes of the responses during fast and slow inhalations of an odor presented at a given concentration; white dots, no statistical difference (p < 0.01, two-sided Wilcoxon rank-sum test). The odor responses of (G) are indicated.

(I) Fraction of concentration responses changing with inhalation speed (red vertical line) and null distribution obtained by shuffling 1,000 times the inhalation speed label for each concentration response.

(J) Absolute change in firing rate due to a 0.01%-to-0.1% change in odor concentration and a slow-to-fast switch in inhalation of the 0.01% odor (n = 477 neuron-odor pairs; only odor-responsive neurons; p < 0.0001, Wilcoxon signed-rank test). Top, probability density function of the two distributions. Bottom, boxplots indicate the median, 25th and 75th percentiles (box edges), and 1.5 times the interquartile range (whiskers) of the two distributions.

(K) Examples of responses from one neuron to different odor concentrations and inhalation speeds. Left, raster plot and PETHs of the responses to 0.01% (light green) and 0.1% (dark green) v/v averaged across all slow inhalations. Right, raster plot and PETHs of the responses to slow (light green) and fast (light purple) inhalations of 0.01% v/v odor.

(L) CDI calculated using concentration responses within and across inhalation speeds (p < 0.0001, Wilcoxon signed-rank test). Same neuron-odor pairs as in (J). Top, probability density function of the two distributions. Bottom, boxplots indicate the median, 25th and 75th percentiles (box edges), and 1.5 times the interquartile range (whiskers) of the two distributions. See also Figure S1.
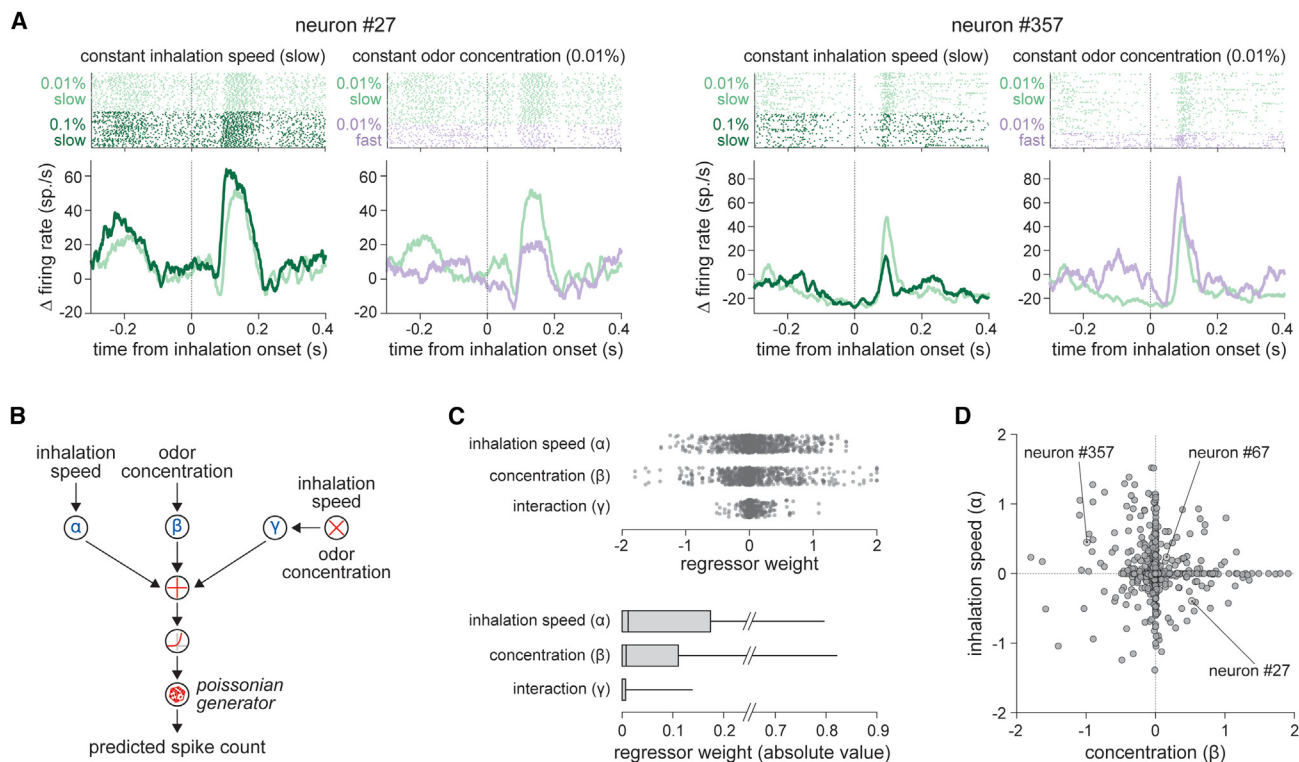
Figure 2. PCx neurons randomly mix olfactory and non-olfactory inputs during inhalations

(A) Examples of responses from two neurons with independent sensitivities to odor concentration and inhalation speed. For each neuron: left, raster plot and PETHs of the responses to 0.01% (light green) and 0.1% (dark green) v/v averaged across all slow inhalations; right, raster plot and PETHs of the responses to slow (light green) and fast (light purple) inhalations of 0.01% v/v odor.

(B) Schematic of the regularized GLM used to predict the odor response based on inhalation speed (slow and fast), odor concentration (0%, 0.01%, 0.1%, 1% v/v), and their interaction.

(C) Top, distribution of the regularized regressor weights for inhalation speed, odor concentration, and their interaction (n = 928 neuron-odor pairs; 2 odors; 464 neurons; 4 mice). Bottom, boxplot of the absolute values of the regularized regressor weights indicating the median, 25th and 75th percentiles (box edges), and the 95th percentile (whisker).

(D) Scatterplot of the concentration and inhalation speed regressor weights. Each data point is a neuron-odor pair (n = 928 neuron-odor pairs; 2 odors; 464 neurons; 4 mice). Neurons #27 and #357 of (A) and neuron #67 of Figure 1K are indicated. See also Figure S2.

concentrations on an inhalation-by-inhalation basis. Figure 1K illustrates this problem in an example PCx neuron. The raster plot and the peri-event time histogram (PETH) in the left column show the responses to two concentrations of the same odor during slow breathing. This neuron generated more action potentials when the odor was delivered at the highest of the two concentrations. The right column shows the responses to the lowest concentration upon a slow or a fast inhalation. The response amplitude to the low concentration during a rapid inhalation was indistinguishable from that measured during a slow inhalation of the more concentrated odor. To assess how varying the inhalation speed affected concentration encoding across all odor-responsive neurons, we calculated a concentration-discriminability index for each neuron (CDI; see STAR Methods). The CDI was computed using the odor responses during slow, fast, or both types of inhalation. Combining responses from slow and fast inhalations decreased the CDI compared with responses observed during uniform inhalation speeds (Figure 1L). This result indicates that varying the inhalation speed adds variability to odor responses in PCx.

PCx neurons randomly mix olfactory and non-olfactory inputs during inhalations

Sniffing could alter odor responses by changing the odorant deposition onto the olfactory epithelium. However, we found odor responses that increased in amplitude with the concentration but decreased with the inhalation speed and others with the opposite pattern (Figure 2A). These observations suggested that odor responses also vary with the inhalation speed because of a non-olfactory input. To assess the relationship between this non-olfactory input and concentration encoding, we fitted a generalized linear model (GLM) to the odor responses of PCx neurons recorded upon different odor concentrations and inhalation speeds. The GLM included three factors: odor concentration (0%, 0.01%, 0.1%, and 1% v/v), inhalation speed (slow or fast), and the interaction between inhalation speed and concentration (Figure 2B). The inhalation speed factor can be interpreted as a non-olfactory input that is combined with the odor input. One way to interpret the multiplicative interaction between inhalation speed and odor concentration is the potential effect of the airflow rate on the concentration profile of the odorant in the

nasal cavity.[4] Other types of interaction cannot be excluded, however. For example, sniffs could be associated with attentional mechanisms that change the gain of the odor response; the interaction weight should capture this effect. To identify the factors that were more relevant for the odor responses of a neuron, we regularized the GLM with an elastic net method. This model explained 91.9% of the variance in the mean number of spikes generated during the first 180 ms of odor inhalation across all neurons.

The GLM analysis revealed that the interaction between inhalation speed and concentration response had a small effect on the odor response amplitude during an inhalation (Figure 2C).

Instead, the non-olfactory input had a more significant additive or subtractive effect (Figure 2C). Importantly, the sign of the weight for the non-olfactory input and the odor concentration factors could differ in the same neuron (Figure 2D). The non-olfactory input caused by a fast inhalation could increase or decrease the odor response amplitude regardless of how the neuron responded to a higher concentration of that odor. Consequently, the combination of non-olfactory and olfactory sensitivities was heterogeneous across PCx neurons (Figure 2D). We similarly found a heterogeneous distribution of non-olfactory sensitivities in RS and FS neurons (Figures S2A and S2B). In addition, different features of the spike waveform could not predict the single or joint olfactory and non-olfactory regressor coefficients of a neuron, suggesting that different cell types have similar encoding properties for the olfactory and non-olfactory inputs (Figure S2C). Finally, restricting the analysis to the early 70 ms of inhalation also gave similar results (Figure S2D). Thus, the non-olfactory input appeared to be the leading cause of the odor response variability observed at different inhalation speeds.

A mechanosensory input signals the nasal airflow rate to the PCx

Sniffing and blowing non-odorized air into the nostrils have been shown to activate the PCx.[16] Therefore, the inhalation speed may affect the odor responses in PCx through an input originating in the nasal cavity. Interestingly, however, the results of the GLM analysis suggested that a sniff could increase the odor response of some neurons but also decrease it in others. To investigate this observation further, we directly assessed how the air passage through the nose affects the spiking activity of PCx neurons.

We first performed a tracheostomy in anesthetized mice to eliminate air passage through the nose during respiration (Figure 3A). This procedure interrupted the normal entrainment of PCx activity to the breathing rhythm as expected (Figure S3A). Then, we stimulated the nasal epithelium with 150-ms-long airflow pulses of odorless air delivered at 1 Hz. We tested five different airflow rates within the range of an awake mouse inhalation.[11,19,30,31] We found that 57.1% of neurons displayed mechanosensory responses, meaning that they encoded the airflow rate. The response latencies varied across neurons, like in normally breathing mice upon inhalation. The responses to the airflow were not uniform across neurons. Some neurons increased their response amplitude as the flow rate increased, whereas others fired fewer action potentials (Figures 3B and

3C). Faster airflow also decreased the response latency without significantly changing the sequential activation order across neurons (Figure 3B; Figure S3B).

That these responses were not an artifact of the artificial stimulation of the nasal cavity in an anesthetized mouse is suggested by the finding of similar mechanosensory tuning curves in awake and normally breathing mice (Figure 3D). For each mouse, we divided the range of the peak airflow rates measured during all inhalations into 10 bins. All bins had an equal number of inhalations. Then, we measured the mean amplitude of the spiking activity during the inhalations within each bin. This analysis revealed that 78.3% of the PCx neurons (77.2% of the odor-responsive neurons) encoded the peak inhalation airflow rate with a monotonic change in spiking activity after the inhalation (Figure 3E). Sorting the airflow tuning curves of all neurons based on their slopes revealed a push-pull organization of the inhalation speed responses again; that is, 36.7% of the neurons increased the amplitude of their responses when the inhalation speed increased, and another 41.7% decreased their responses (Figure 3F).

What was the source of the mechanosensory input? During each inhalation, OSNs can be excited by background odors or pressure changes, and blocking OSNs' responses disrupts the typical synchronization between respiration and the local field potential recorded in the OB.[20] Thus, OSNs could provide mechanosensory information to the PCx. Nonetheless, our results could not exclude the possibility that trigeminal sensation could also provide nasal airflow information to the PCx. For example, the trigeminal input may afford sensitivity to the airflow rate, and the OSN input may only give a bulk activation indicating the inhalation onset. Intriguingly, a branch of the trigeminal nerve called the anterior ethmoidal nerve (AEN) innervates the olfactory epithelium and the OB as well.[32] The fibers of the AEN respond to chemical and mechanical stimulation.[33] Therefore, the AEN afferences could sense the airflow rate inside the nasal cavity and broadcast this information to the PCx through the OBs. To test this possibility, we sectioned the AEN (Figure S3C). In a subset of mice, we occluded the contralateral nostril to prevent information leakage from the contralateral side. Severing the AEN left intact the responses of PCx neurons to inhalations. The tuning curves for the airflow rate after the neurectomy remained similar to those of control mice (Figures S3D and S3E). These data indicate that PCx neurons encode the inhalation airflow rate in the nasal cavity through a mechanosensory input that most likely arises from the OSNs.

A top-down input may supply behavioral state information during a sniff

While the above results show that the PCx encodes the airflow rate inside the nasal cavity, they do not eliminate the possibility that top-down inputs could also account for the activity changes caused by faster sniffing in PCx. Sniffing characterizes active exploration and arousal states.[6,29] Therefore, top-down and neuromodulatory inputs associated with those behavioral states may affect the activity of PCx neurons during a sniff. The responses to these inputs could be hard to distinguish in normal conditions because they would likely be mixed with the mechanosensory responses. Moreover, although our artificial
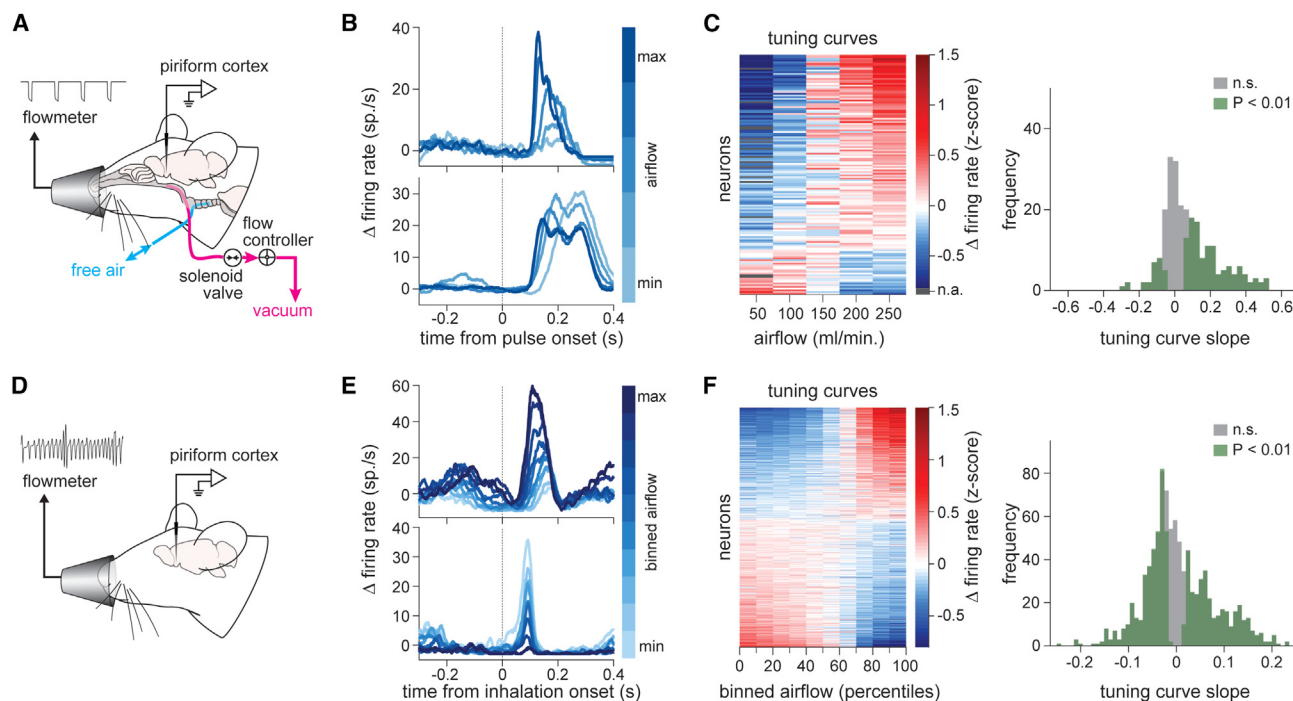
Figure 3. A mechanosensory input signals the nasal airflow rate to the PCx
(A) Experimental setup for artificial airflow stimulation of the nasal cavity in anesthetized mice.
(B) PETHs of two example neurons responding to five different airflow rates.
(C) Left, raster map of airflow rate tuning curves (n = 144 airflow-tuned neurons of 252; 3 mice). Right, distribution of the slopes of the airflow tuning curves. Shaded area, slopes significantly different from zero. Positive slope, 117 neurons; negative slope, 27 neurons (p < 0.01, t test).
(D) Experimental setup for PCx recordings paired with spontaneous breathing monitoring in awake mice in the absence of odors.
(E) PETHs of two example neurons responding to 10 different peak airflow rates.
(F) Left, raster map of the tuning curves for the peak airflow rate (n = 748 peak-rate-tuned neurons of 955; 10 mice). Right, distribution of the tuning curve slopes like in (C). Positive slope, 350 neurons; negative slope, 398 neurons (p < 0.01, t test). See also Figure S3.

ventilation experiments uncoupled the respiratory activity from the mechanical stimulation of the nasal cavity, they also prevented volitional sniffing because they were performed under anesthesia. To isolate the possible effect of top-down inputs during a sniff, we removed both OBs in a group of mice and recorded the activity of PCx neurons during wakefulness (Figure 4A). We examined the responses to the first fast sniff after a sequence of at least five slow inhalations and to a regular slow inhalation in the absence of odors.

In bulbectomized mice, PCx neurons were unresponsive to odors (Figure S4A). Moreover, the population activity did not encode the inhalation phase (Figure 4B; Figure S4B). These results were consistent with a block of the peripheral inputs to the PCx. Nonetheless, 15.7% of PCx neurons exhibited increased spiking activity during fast sniffs compared with normal inhalations (see example neuron in Figure 4C). For comparison, this proportion was 29.7% in control mice. However, the sniff-induced activity in bulbectomized mice was smaller in amplitude and more variable across sniffs than in control mice (Figures 4D–4F). Correspondingly, while a linear classifier could differentiate a sniff from a regular inhalation based on PCx activity in both groups, its accuracy was notably reduced post-bulbectomy (Figure 4G). Remarkably, the sniff-induced activity observed in the bulbectomized

mice seemed to start rising several tens of milliseconds before the nominal onset of the sniff. Since responses to slow inhalations were absent in these neurons, this peri-sniff increase in spiking activity could not be attributed to the previous inhalation.

The increase in neural activity around the onset of a fast sniff was not specific to the PCx. We found a similar peri-sniff signal in the motor cortex (MCx). Here, a slow inhalation modulated the activity of 5.8% of neurons (see STAR Methods). In contrast, 17.1% of MCx neurons showed a significant peri-sniff increase in spiking activity akin to that observed in PCx following bulbectomy (Figures S4C–S4E). Together, these data suggest the hypothesis that sniffs may be preceded by a global top-down signal that may further affect odor responses in PCx.

Odor information and inhalation information are independent
An important result of the GLM analysis was that odor and inhalation speed sensitivities appeared randomly distributed among odor-responsive PCx neurons. This heterogeneity in sensitivity raises the possibility that the representations of the two modalities do not interfere at the population level (see STAR Methods for a formal derivation in linear encoding systems). PCx represents the identity and concentration of a given odor with a
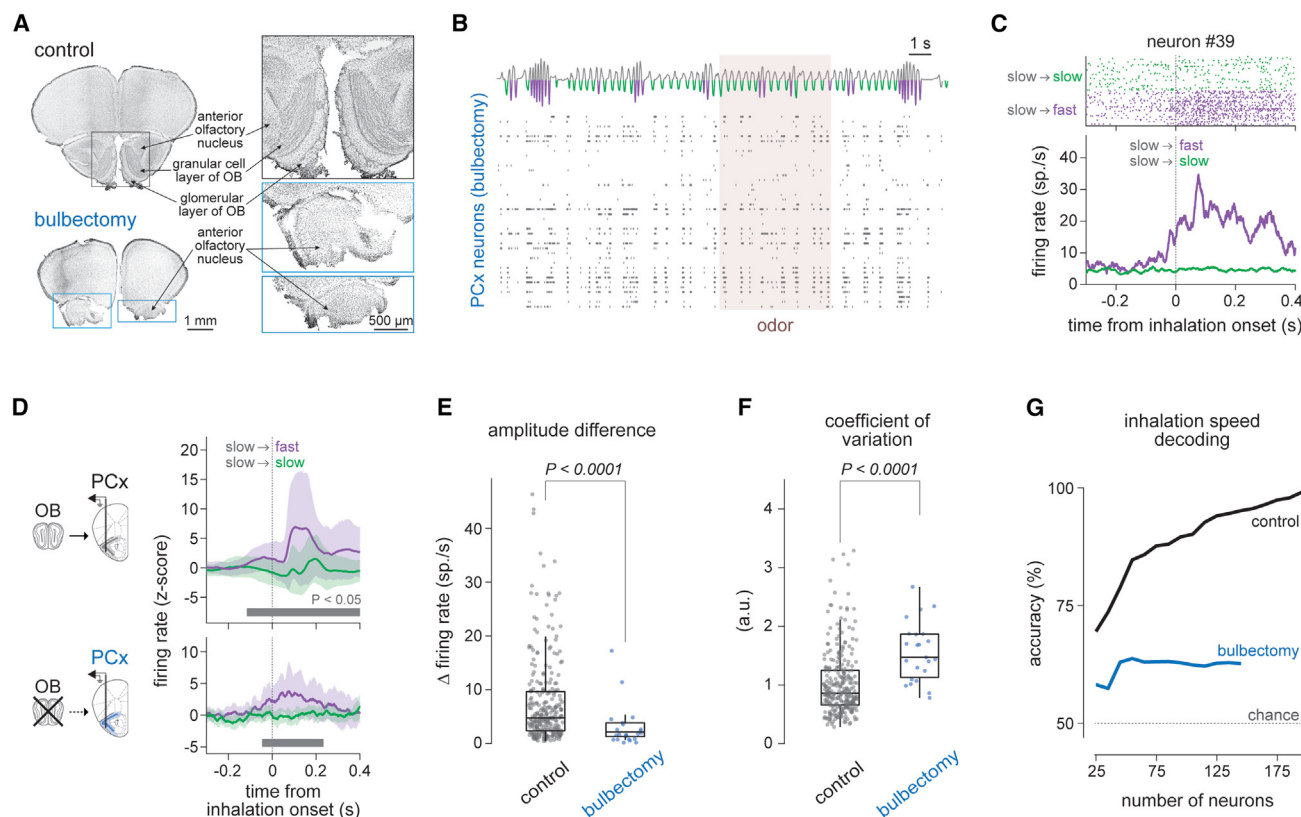
Figure 4. A top-down input may supply behavioral state information during a sniff

(A) Coronal section images in a representative control (top) and bulbectomized (bottom) mouse. Scale bar: 1 mm (insets: 500 μm).

(B) Example of simultaneous PCx activity and respiratory airflow rate in an awake mouse after a bulbectomy. External flow sensor signal (top) and spiking raster plot (bottom). Shaded area, odor period (5 s).

(C) Spiking activity during slow and fast inhalations in an example neuron after a bulbectomy. Raster plot (top) and PETH (bottom) are shown. The responses to the first sniff after at least five slow inhalations and to a slow inhalation are color coded in purple and green, respectively.

(D) Average PETHs of neurons preferring a sniff over a slow inhalation in mice with intact OBs (top; 284 of 955 neurons; 10 mice) and in bulbectomized mice (bottom; 23 of 153 neurons; 4 mice). Shaded area, mean ± SEM. The bar below the PETH indicates when the sniff responses are significantly bigger than the responses to a regular inhalation (Benjamini-Hochberg adjusted p < 0.05, one-sided t test).

(E) Difference between the amplitudes of the responses to the first sniff and a slow inhalation in control and bulbectomized mice (p = 0.0002; two-tailed t test with unequal variances). Boxplots indicate the median, 25th and 75th percentiles (box edges), and 1.5 times the interquartile range (whiskers).

(F) Coefficient of variation of the response amplitude across first sniffs in control and bulbectomized mice (p < 0.0001; two-tailed t test). Boxplots indicate the median, 25th and 75th percentiles (box edges), and 1.5 times the interquartile range (whiskers).

(G) Decoding accuracy of inhalation speed as a function of the neurons included in the analysis; classifiers used the activity of a pseudo-population of PCx neurons in the control condition (black line) and after bulbectomy (blue line). See also Figure S4.

specific pattern of activation of ensembles of neurons or, equivalently, with population vectors.[24,25,28,34,35] Figure 5A shows the principal-component analysis (PCA) embedding of the pseudo-population response vectors to three concentrations (0.01%, 0.1%, and 1% v/v) of an odor upon slow and fast inhalations (see also Figure S5A for the inhalation-by-inhalation population responses in individual mice and Figure S5B for a different odor). Increases in concentration result in scaling the population vector magnitude without changing vector direction, as already observed in prior work.[22,23] Since the sniff response of an odor-responsive neuron weakly correlated with that of other odor-responsive neurons, the direction of the population vector response to an increase in inhalation speed did not overlap with the direction of the concentration population response. In other words, inhalation speed information did not affect the encoding of the odor concentration.

To confirm this qualitative observation, we set out to decode either the inhalation speed or the odor concentration from the projections of the PCx responses on the first 15 PCs (Figure 5B; Figures S5C and S5D). Linear decoders—namely, linear support vector machine (lSVM) classifiers—could discriminate the inhalation speed with high accuracy using the projection of neural activity onto the first PC. In contrast, decoders could not classify an odor concentration using only the activity explained by the first PC. Moreover, decoders could not classify an odor identity using only the activity explained by the first PC (Figure S5E), further suggesting that the variance explained by the first PC does not encode olfactory information. Conversely, linear classifiers
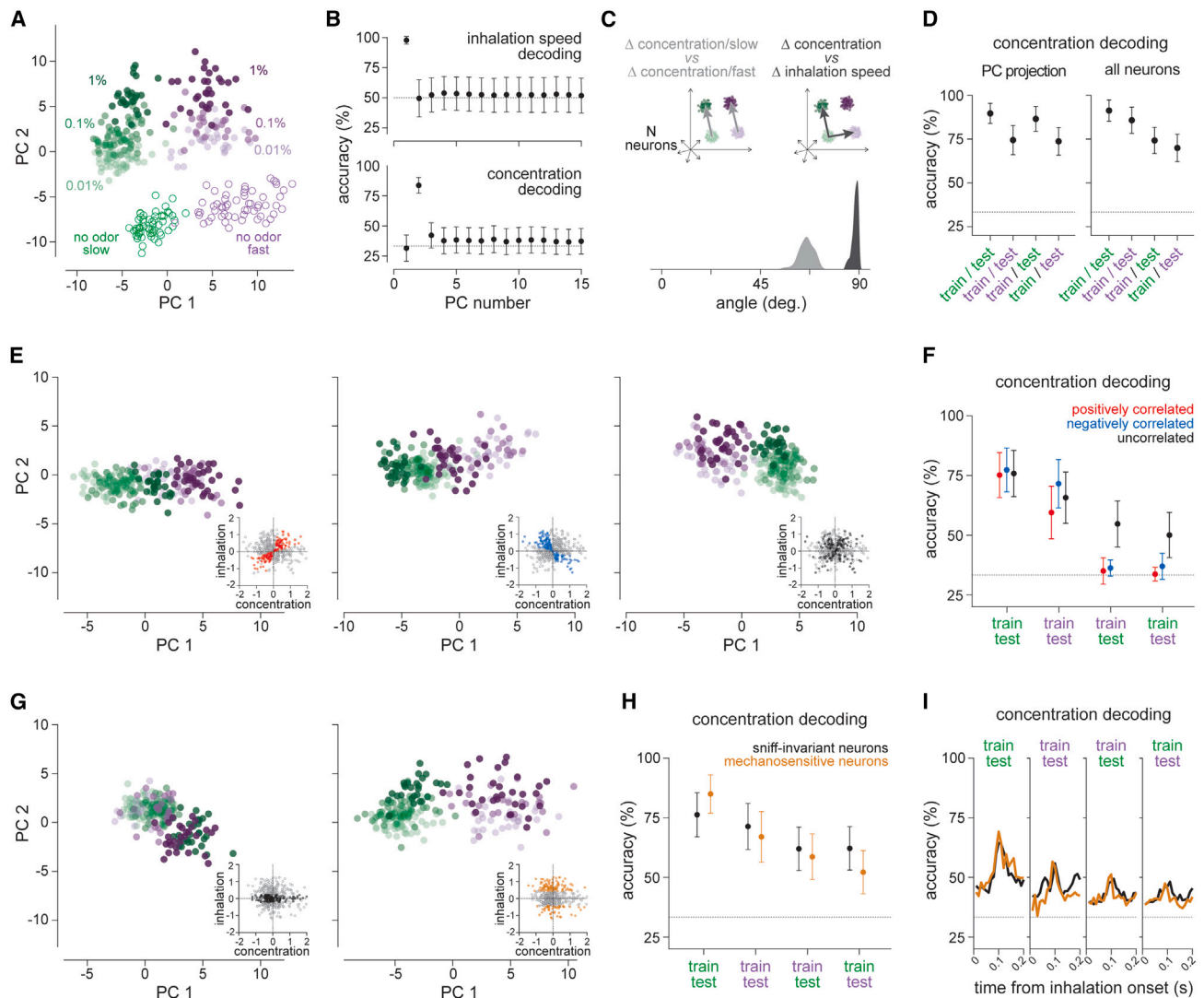
Figure 5. Odor information and inhalation information are independent

(A) PCA embedding of pseudo-population responses (464 neurons, 4 mice) to three different concentrations of an example odor during slow (green) and fast (purple) inhalations. Each dot is a response in a 180 ms window starting at inhalation onset. Empty dots represent inhalation responses in the absence of odors. A random sample of all responses is shown.

(B) Decoding accuracy of inhalation speed (top) and odor concentration (bottom) using the projection of the pseudo-population odor responses in (A) on each of the first 15 PCs. Mean ± SD is shown.

(C) Angle between vector pairs representing concentration changes (light gray) and vector pairs representing a concentration change and an inhalation speed change (dark gray).

(D) Left, concentration decoding accuracy of *cis-* and *trans*-decoders using the pseudo-population response projections onto the second and third PCs. Right, concentration decoding accuracy of *cis-* and *trans*-decoders using non-reduced population responses. Mean ± SD is shown.

(E) PCA embedding of concentration responses for three pseudo-populations with positive (left), negative (center), and no correlation (right) between inhalation and concentration sensitivity. Insets: scatterplots of inhalation and concentration regression coefficients for all the neurons of the same pseudo-population used in (A). Red, neurons with positive correlation; blue, neurons with negative correlation; black, neurons without correlation. An equal number of neurons was randomly sampled from each sub-population (n = 143 neurons). A random sample of all responses is shown.

(F) Concentration decoding accuracy of *cis-* and *trans*-decoders using the three neural sub-populations in (E). Mean ± SD is shown.

(G) PCA embeddings of concentration responses using a pseudo-population with (left) and without (right) sniff-invariant neurons. Insets: scatterplots of the inhalation and concentration regression coefficients for all the neurons of the same pseudo-population used in (A). The subset of neurons in the population response vector is highlighted by color: black, sniff-invariant neurons; orange, mechanosensitive neurons. An equal number of neurons was randomly sampled from each sub-population (n = 143 neurons). A random sample of all responses is shown.

(H) Concentration decoding accuracy of *cis-* and *trans*-decoders inhalation speed using sniff-invariant (black) and mechanosensitive (orange) neurons. Mean ± SD is shown.

(I) Concentration decoding accuracy within and across inhalation speed over the time course of an inhalation (p > 0.05; two-way ANOVA). An equal number of neurons was randomly sampled from each sub-population (n = 143 neurons). See also Figure S5.

decoded the odor concentration and identity with high accuracy when they used neural activity along the second and third PCs (Figure 5B; Figures S5C and S5E). However, classifiers could not discriminate the inhalation speed using the second and subsequent PCs.

Importantly, we expected that how PCx encoded odor concentration would not depend on inhalation speed. To test this hypothesis, we used linear discriminant analysis to find two directions in the population neural activity that best tell odor concentrations apart during slow or fast breathing. We found that, even though these two directions were different (as expected, given the high dimensionality of the population response), they were more similar than the directions that tell how fast a mouse breathes in apart from how concentrated the odor is (Figure 5C).

The distributed representation of odor concentration is sniff invariant

These results suggested that the cortical representation of odor concentration could be sniff invariant. We thus trained an ISVM to decode an odor concentration using a subset of slow or fast inhalations; then, we tested the performance of the same decoder using held-out inhalations with the same (*cis-*) or other speed (*trans-*decoding). A decoder using PCx response projections on the second and third PCs exhibited similar *cis-* and *trans-*decoding performances, suggesting that PCx has sniff-invariant representations of odor concentration (Figure 5D; Figures S5F and S5G). Next, we tested the linear decoders on the untransformed PCx responses, thus removing the possibility that the decoder could leverage the denoised representations provided by PCA; this *trans-*decoder could still predict the odor concentration, generalizing across inhalation speeds (Figure 5D; Figure S5F). We observed similar results when the decoders used spike counts summed over 70 or 180 ms windows and spike counts for concatenated 10 ms or 10° bins over a respiratory cycle (Figures S5G and S5H).

How well the concentration information was preserved across inhalation speeds was determined by how heterogeneous the combination of inhalation speed and olfactory tuning was across neurons. To confirm this, we performed PCA and decoding analysis on neural sub-populations with correlated sensitivity to non-olfactory and olfactory inputs, thus removing the heterogeneous distribution of non-olfactory and olfactory responses. PCA embeddings of the odor responses showed that representations of odor concentrations become ambiguous across inhalation speeds in these sub-populations (Figure 5E). Thus, a *trans-*decoder performed at the chance level if it could use only the activity of a neural population with correlated sensitivity for non-olfactory and olfactory inputs (Figure 5F). Instead, using a population with uncorrelated selectivity disentangled the representations of inhalation speed and odor concentration, thus allowing a *trans-*decoder to distinguish odor concentrations across inhalation speeds (Figures 5E and 5F).

Our dataset also included neurons that did not change their odor responses with the inhalation speed. A downstream reader could privilege the information from these sniff-invariant neurons to obtain a stable readout of the odor concentration across inhalation speeds. We determined whether a population of neurons insensitive to the inhalation speed could afford more sniff-invariant information than the rest of the neural population. To select the sniff-invariant neurons, we assessed the sensitivity to the inhalation speed of each neuron in our dataset. To this aim, we fitted the inhalation-by-inhalation odor responses with a linear regression model with a concentration and an inhalation speed regressor. Neurons with an inhalation speed regressor coefficient within 0 ± 0.75 standard deviations were included in the sniff-invariant population. In contrast, an equal number of neurons with an inhalation speed regressor coefficient beyond ±1.5 standard deviations from zero were included in a population that we denoted as mechanosensitive (Figure 5G). The two populations of sniff-insensitive and mechanosensitive neurons had similar distributions of concentration regressor coefficients (Figure S5I). We compared the classification accuracies of linear *trans-*decoders using sniff-invariant and mechanosensitive populations. This analysis revealed that a population of mechanosensitive neurons carries at least as much sniff-invariant information as a population of only sniff-insensitive neurons (Figure 5H).

We also examined the possibility that sniff-insensitive neurons could provide more sniff-invariant information than mechanosensitive neurons during the earliest part of an inhalation. To this aim, we employed the *cis-* and *trans-*decoding approach in 20 consecutive time bins (10 ms/bin), tiling the first 200 ms of an inhalation. Linear decoders using only mechanosensitive or sniff-insensitive neurons performed similarly throughout this inhalation window (Figure 5I). Together, these results confirm that sniff-invariant concentration information is distributed across the activity pattern of the odor-responsive PCx neural population.

Airflow information affords tolerance to flow-dependent concentration fluctuations

Our data indicated that adding a mechanosensory response to olfactory responses does not significantly alter the representation of odor concentration in PCx. In fact, adding the inhalation speed information teases apart the representations of the odor concentration under different inhalation speeds. Therefore, this coding strategy may allow a linear decoder to distinguish an environmental increase in concentration from one induced by a nasal airflow change. This way, the decoder can learn that the two activity patterns evoked by an odor upon slow and fast inhalations represent, in fact, the same concentration (Figure 6A). To test the robustness of this coding strategy, we simulated the responses of a population of neurons with varying levels of inhalation speed-dependent concentration change and mechanosensory input. To generate the surrogate distribution of responses, we used the odor and inhalation covariate weights obtained by fitting our recorded neural responses with a linear regression model. We simulated different levels of interaction between airflow and odorant deposition by assuming that the inhalation-driven change in concentration (ΔIC) is proportional to the initial concentration and the inhalation speed, as per prior fluid dynamics modeling[4] (see STAR Methods). We varied ΔIC over a 2-fold range to approximate the natural nasal airflow rate range.[36] PCA embedding showed that odor representations were ambiguous in this simulated population when there was no inhalation input (Figure 6B); for example, an increase in odor concentration could not be distinguished
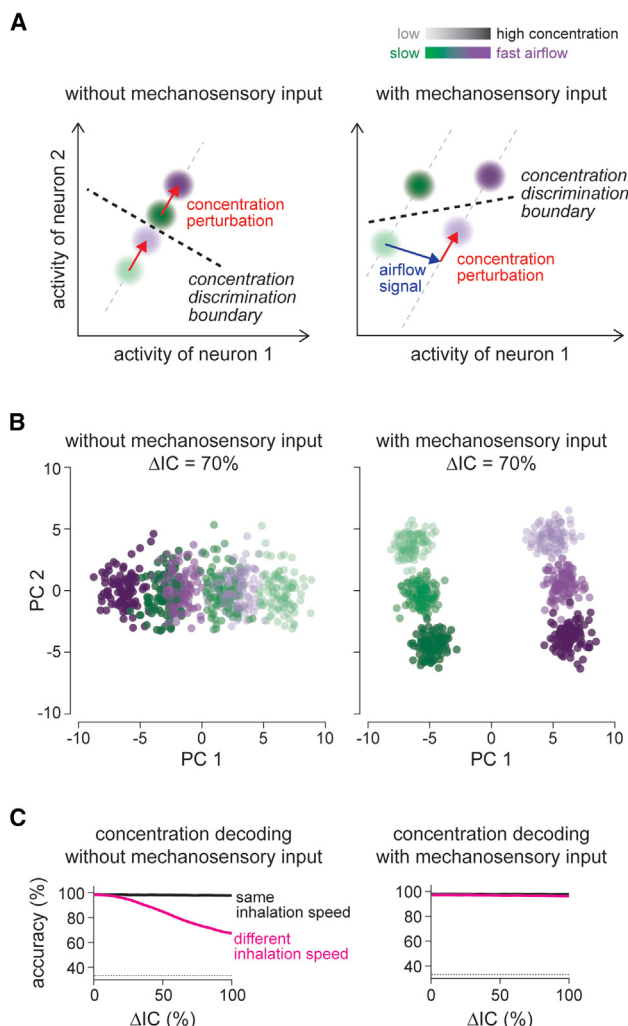
A

B

C

Figure 6. Airflow information affords tolerance to flow-dependent concentration fluctuations

(A) Example of how adding an independent mechanosensory signal distinguishes the inhalation-induced concentration fluctuation from an inhalation-independent change in concentration.

(B) Inferred effect of the mechanosensory input on the concentration representation in the presence of an inhalation-driven alteration of the odor concentration. Left, PCA embedding of population concentration responses with a 70% inhalation-driven concentration change (ΔIC) and without inhalation input. Right, PCA embedding of population concentration responses with a 70% ΔIC and mechanosensory input.

(C) Concentration decoding accuracy for increasing levels of inhalation-dependent ΔIC without (left) and with (right) mechanosensory input within (black) or across (magenta) different inhalation speeds.

from an increase in inhalation speed. Consistently, decoders trained on the responses during slow and fast inhalations classified the odor concentration worse than decoders trained using only one inhalation speed as the simulated influence of the airflow on the concentration increased (Figure 6C). However, supplementing this population with mechanosensory responses was sufficient to reduce ambiguity and retrieve the actual concentration for any ΔIC (Figures 6B and 6C).

DISCUSSION

Our experiments indicate that the PCx encodes precise information about inhalation dynamics through a signal generated by the nasal air pressure or background odors. The airflow rate tuning curves that we measured showed a push-pull arrangement across the population of PCx neurons, meaning that a faster inhalation increased the response of some neurons while decreasing that of others. Such a distribution of tuning curves is known to stabilize the average firing rate and keep the information rate constant across the full range of nasal airflow velocities experienced by the mouse. Combined with a random sampling of odor,[26,27,37] such a bidirectional organization expands the possible combinations of sensitivities to the odor and inhalation inputs, warranting a more robust tolerance to varying inhalation speeds in PCx.

The information provided by the airflow signal differentiates concentration representations upon different inhalation speeds. However, it cannot correct the concentration change caused by varying the inhalation speed in and by itself. Although the mechanosensory feedback is the same regardless of which odor an animal smells, the concentration change caused by a change in inhalation speed is likely different for different scents. Indeed, how much odorant crosses the olfactory mucosa depends on the airflow velocity and the odorant's air-water partition coefficient.[38,39] Thus, the correspondence between two representations of the same environmental concentration upon two inhalation speeds has to be learned from experience. In most instances, the concentration of an odorous source (for example, the octanal molecules in an orange peel) tends to be stable during an olfactory experience. We hypothesize that the brain could learn to generalize across inhalation speeds by taking advantage of the temporal contiguity of an odorant source during consecutive inhalations. A similar, unsupervised learning strategy might work even in a more naturalistic scenario involving variable odor plumes and odorant mixtures. Further work will be required to investigate how the olfactory circuits exploit the spatiotemporal statistics of the olfactory environment and fully understand the relationship between experience and tolerance to self-generated stimulus variability.

Our work illustrates a solution to the sensory disturbances caused by movements. This solution does not rely on inhibitory corollary discharges but leverages the computational benefits of population codes. Such a coding strategy is so general that it is likely to be used by other sensory systems. Indeed, the coexistence of independent motion and sensory signals is not a unique feature of the olfactory system. Orthogonal dimensions for encoding movements and sensory stimuli have been found in other sensory cortices, such as the primary visual cortex (V1).[40–42] However, the function of these movement signals is a matter of debate.[43,44] In recent work, it was observed that V1 neurons independently encode the direction of a drifting visual grating and a saccade. It was proposed that this encoding strategy may "scramble" the image representation during the saccade, thus suppressing the perception of the retinal image drift caused by the saccade.[45] Here, we observe that the motion-related signal does not destroy the olfactory information in PCx. Rather, the sniff signal lawfully reconfigures the concentration representations according to the nasal airflow. Thus, a

downstream area can learn an optimal decoding scheme that retrieves the true concentration, like with a conversion chart (see the model in Figure 6A). The motion signals in V1 could have a similar function. Interestingly, psychophysical experiments in humans suggest that reafferent mechanosensory signals reduce the perceived extent of the visual smear generated by passive head and eye movements;[46] notably, these observations also offer a functional interpretation of the additive inputs that the mouse V1 receives from the vestibular system.[47–49] Mechanosensation is the analysis of movement; thus, embedding independent mechanosensory reafferences into distributed sensory codes could be a canonical neural design to parse and reject the consequences of sensory organ movements on sensation.

Limitations of the study

We observed an increase in spiking activity around the onset of rapid sniffs in bulbectomized mice, suggesting the influence of top-down input on PCx activity. Although the possibility of residual peripheral input cannot be entirely ruled out, no clear evidence of remaining glomeruli was found in postmortem histological examination of bulbectomized mice. However, undetected afferents during electrophysiological recording, subsequently destroyed during sectioning, cannot be discounted. Despite the absence of PCx responses to odors or inhalation phase encoding post-bulbectomy, the heightened mechanosensory stimulation from rapid sniffs may account for the observed response. Notably, however, the response initiated before the sniff, arguing against a reafferent origin. Moreover, we observed a similar peri-sniff activity in a region devoid of OB inputs, such as the MCx, suggesting a top-down origin of the input. Identifying the precise source of the presumed top-down modulation driving the sniff response remains a task for future investigations.

Our GLM analysis revealed heterogeneous tuning to odor concentration and inhalation speed among RS and FS neurons. Moreover, the spike waveform of a unit could not predict the joint encoding of the olfactory and inhalation-speed input. However, the PCx's vast neural diversity[50] suggests that our neuron sorting criteria, based on spike waveform features, may be overly simplistic to discerning cell-type-specific tuning differences. Future work could employ more granular classification methods, such as molecular markers, to refine our understanding of the role of inhalation signals in PCx odor processing.

We demonstrated that a linear decoder may leverage the information about the inhalation speed to correct for the sniff-driven concentration increase. Still, it remains speculative whether mice employ such a compensatory mechanism. More generally, we posited that variable inhalation speeds pose a challenge for maintaining consistent olfactory representations. However, such a stimulus modulation may be actually a feature that allows the brain to form predictive models of the environment.[44] By changing the inhalation speed, an animal could be actively testing these models against incoming sensory information to enhance the accuracy of odor perception. Critically, our analyses show that all information is preserved in the PCx, which would not be possible if an inhibitory input suppressed the sensory consequences of sniffing. This way, an animal could use the benefits of active sensing without incurring a deterioration of the acquired information.

STAR★METHODS

Detailed methods are provided in the online version of this paper and include the following:

- KEY RESOURCES TABLE
- RESOURCE AVAILABILITY
  - Lead contact
  - Materials availability
  - Data and code availability
- EXPERIMENTAL MODEL AND STUDY PARTICIPANT DETAILS
  - Mice
- METHOD DETAILS
  - Surgical procedures
  - Habituation to the experimental rig
  - Stereotaxic probe insertion
  - Experimental signals
  - Odor delivery
  - Artificial mechanical stimulation
  - Histology
  - Experimental design
- QUANTIFICATION AND STATISTICAL ANALYSIS
  - Analysis of the breathing signal
  - Inhalation clustering
  - Spike sorting and inclusion criteria
  - Analysis of sniff-by-sniff responses
  - Concentration discrimination index
  - Tuning curves
  - Encoding models
  - Prediction of encoding properties from waveforms
  - Pseudo-population response matrix
  - PCA embeddings
  - Angle between encoding axes
  - Inhalation speed decoding
  - Concentration decoding
  - Inhalation phase decoding
  - Simulation of sniff-induced concentration changes
  - Geometrical proof
  - Statistical tests

AUTHOR CONTRIBUTIONS

Conceptualization, G.I.; methodology, F.M., P.P., A.A.D., and G.I.; software, A.A.D., P.P., L.P., and G.I.; formal analysis, A.A.D., P.P., L.P., E.P., and G.I.; investigation, F.M., P.P., and G.I.; resources, G.I.; data curation, A.A.D. and P.P.; writing, G.I.; visualization, P.P. and G.I.; supervision, G.I.; project administration, G.I.; funding acquisition, G.I.

REFERENCES

1. Crapse, T.B., and Sommer, M.A. (2008). Corollary discharge across the animal kingdom. Nat. Rev. Neurosci. *9*, 587–600. https://doi.org/10.1038/nrn2457.

2. Teghtsoonian, R., Teghtsoonian, M., Berglund, B., and Berglund, U. (1978). Invariance of odor strength with sniff vigor: an olfactory analogue to size constancy. J. Exp. Psychol. Hum. Percept. Perform. *4*, 144–152. https://doi.org/10.1037//0096-1523.4.1.144.

3. Mainland, J., and Sobel, N. (2006). The sniff is part of the olfactory percept. Chem. Senses *31*, 181–196. https://doi.org/10.1093/chemse/bjj012.

4. Shusterman, R., Sirotin, Y.B., Smear, M.C., Ahmadian, Y., and Rinberg, D. (2018). Sniff Invariant Odor Coding. eNeuro *5*. https://doi.org/10.1523/ENEURO.0149-18.2018.

5. Jordan, R., Kollo, M., and Schaefer, A.T. (2018). Sniffing Fast: Paradoxical Effects on Odor Concentration Discrimination at the Levels of Olfactory Bulb Output and Behavior. eNeuro *5*. https://doi.org/10.1523/eneuro.0148-18.2018.

6. Kepecs, A., Uchida, N., and Mainen, Z.F. (2006). The Sniff as a Unit of Olfactory Processing. Chem. Senses *31*, 167–179. https://doi.org/10.1093/chemse/bjj016.

7. Catania, K.C. (2013). Stereo and serial sniffing guide navigation to an odour source in a mammal. Nat. Commun. *4*, 1441. https://doi.org/10.1038/ncomms2444.

8. Ache, B.W., Hein, A.M., Bobkov, Y.V., and Principe, J.C. (2016). Smelling Time: A Neural Basis for Olfactory Scene Analysis. Trends Neurosci. *39*, 649–655. https://doi.org/10.1016/j.tins.2016.08.002.

9. Parabucki, A., Bizer, A., Morris, G., Munoz, A.E., Bala, A.D.S., Smear, M., and Shusterman, R. (2019). Odor Concentration Change Coding in the Olfactory Bulb. eNeuro *6*. https://doi.org/10.1523/ENEURO.0396-18.2019.

10. Carey, R.M., Verhagen, J.V., Wesson, D.W., Pírez, N., and Wachowiak, M. (2009). Temporal Structure of Receptor Neuron Input to the Olfactory Bulb Imaged in Behaving Rats. J. Neurophysiol. *101*, 1073–1088. https://doi.org/10.1152/jn.90902.2008.

11. Verhagen, J.V., Wesson, D.W., Netoff, T.I., White, J.A., and Wachowiak, M. (2007). Sniffing controls an adaptive filter of sensory input to the olfactory bulb. Nat. Neurosci. *10*, 631–639. https://doi.org/10.1038/nn1892.

12. Ghatpande, A.S., and Reisert, J. (2011). Olfactory receptor neuron responses coding for rapid odour sampling. J. Physiol. *589*, 2261–2273. https://doi.org/10.1113/jphysiol.2010.203687.

13. Adrian, E.D. (1950). The electrical activity of the mammalian olfactory bulb. Electroencephalogr. Clin. Neurophysiol. *2*, 377–388. https://doi.org/10.1016/0013-4694(50)90075-7.

14. Macrides, F., and Chorover, S.L. (1972). Olfactory bulb units: activity correlated with inhalation cycles and odor quality. Science *175*, 84–87. https://doi.org/10.1126/science.175.4017.84.

15. Cang, J., and Isaacson, J.S. (2003). In vivo Whole-Cell Recording of Odor-Evoked Synaptic Transmission in the Rat Olfactory Bulb. J. Neurosci. *23*, 4108–4116. https://doi.org/10.1523/JNEUROSCI.23-10-04108.2003.

16. Sobel, N., Prabhakaran, V., Desmond, J.E., Glover, G.H., Goode, R.L., Sullivan, E.V., and Gabrieli, J.D. (1998). Sniffing and smelling: separate subsystems in the human olfactory cortex. Nature *392*, 282–286. https://doi.org/10.1038/32654.

17. Díaz-Quesada, M., Youngstrom, I.A., Tsuno, Y., Hansen, K.R., Economo, M.N., and Wachowiak, M. (2018). Inhalation Frequency Controls Reformatting of Mitral/Tufted Cell Odor Representations in the Olfactory Bulb. J. Neurosci. *38*, 2189–2206. https://doi.org/10.1523/JNEUROSCI.0714-17.2018.

18. Fontanini, A., Spano, P., and Bower, J.M. (2003). Ketamine-Xylazine-Induced Slow (< 1.5 Hz) Oscillations in the Rat Piriform (Olfactory) Cortex Are Functionally Correlated with Respiration. J. Neurosci. *23*, 7993–8001. https://doi.org/10.1523/jneurosci.23-22-07993.2003.

19. Iwata, R., Kiyonari, H., and Imai, T. (2017). Mechanosensory-Based Phase Coding of Odor Identity in the Olfactory Bulb. Neuron *96*, 1139–1152.e7. https://doi.org/10.1016/j.neuron.2017.11.008.

20. Grosmaitre, X., Santarelli, L.C., Tan, J., Luo, M., and Ma, M. (2007). Dual functions of mammalian olfactory sensory neurons as odor detectors and mechanical sensors. Nat. Neurosci. *10*, 348–354. https://doi.org/10.1038/nn1856.

21. Connelly, T., Yu, Y., Grosmaitre, X., Wang, J., Santarelli, L.C., Savigner, A., Qiao, X., Wang, Z., Storm, D.R., and Ma, M. (2015). G protein-coupled odorant receptors underlie mechanosensitivity in mammalian olfactory sensory neurons. Proc. Natl. Acad. Sci. USA *112*, 590–595. https://doi.org/10.1073/pnas.1418515112.

22. Iurilli, G., and Datta, S.R. (2017). Population Coding in an Innately Relevant Olfactory Area. Neuron *93*, 1180–1197.e7. https://doi.org/10.1016/j.neuron.2017.02.010.

23. Bolding, K.A., and Franks, K.M. (2018). Recurrent cortical circuits implement concentration-invariant odor coding. Science *361*, eaat6904. https://doi.org/10.1101/294132.

24. Miura, K., Mainen, Z.F., and Uchida, N. (2012). Odor Representations in Olfactory Cortex: Distributed Rate Coding and Decorrelated Population Activity. Neuron *74*, 1087–1098. https://doi.org/10.1016/j.neuron.2012.04.021.

25. Kadohisa, M., and Wilson, D.A. (2006). Separate encoding of identity and similarity of complex familiar odors in piriform cortex. Proc. Natl. Acad. Sci. USA *103*, 15206–15211. https://doi.org/10.1073/pnas.0604313103.

26. Stettler, D.D., and Axel, R. (2009). Representations of odor in the piriform cortex. Neuron *63*, 854–864. https://doi.org/10.1016/j.neuron.2009.09.005.

27. Wilson, D.A., and Sullivan, R.M. (2011). Cortical processing of odor objects. Neuron *72*, 506–519. https://doi.org/10.1016/j.neuron.2011.10.027.

28. Schoonover, C.E., Ohashi, S.N., Axel, R., and Fink, A.J.P. (2021). Representational drift in primary olfactory cortex. Nature *594*, 541–546. https://doi.org/10.1038/s41586-021-03628-7.

29. Wachowiak, M. (2011). All in a Sniff: Olfaction as a Model for Active Sensing. Neuron *71*, 962–973. https://doi.org/10.1016/j.neuron.2011.08.030.

30. Kepecs, A., Uchida, N., and Mainen, Z.F. (2007). Rapid and Precise Control of Sniffing During Olfactory Discrimination in Rats. J. Neurophysiol. *98*, 205–213. https://doi.org/10.1152/jn.00071.2007.

31. Oka, Y., Takai, Y., and Touhara, K. (2009). Nasal Airflow Rate Affects the Sensitivity and Pattern of Glomerular Odorant Responses in the Mouse Olfactory Bulb. J. Neurosci. *29*, 12070–12078. https://doi.org/10.1523/JNEUROSCI.1415-09.2009.

32. Schaefer, M.L., Böttger, B., Silver, W.L., and Finger, T.E. (2002). Trigeminal collaterals in the nasal epithelium and olfactory bulb: a potential route for direct modulation of olfactory information by trigeminal stimuli. J. Comp. Neurol. *444*, 221–226. https://doi.org/10.1002/cne.10143.

33. Maurer, M., Papotto, N., Sertel-Nakajima, J., Schueler, M., De Col, R., Möhrlen, F., Messlinger, K., Frings, S., and Carr, R.W. (2019). Photoactivation of olfactory sensory neurons does not affect action potential conduction in individual trigeminal sensory axons innervating the rodent nasal cavity. PLoS One *14*, e0211175. https://doi.org/10.1371/journal.pone.0211175.

34. Pashkovski, S.L., Iurilli, G., Brann, D., Chicharro, D., Drummey, K., Franks, K.M., Panzeri, S., and Datta, S.R. (2020). Structure and flexibility in cortical representations of odour space. Nature *583*, 253–258. https://doi.org/10.1038/s41586-020-2451-1.

35. Bolding, K.A., and Franks, K.M. (2017). Complementary codes for odor identity and intensity in olfactory cortex. Elife *6*, e22630. https://doi.org/10.7554/eLife.22630.

36. Youngentob, S.L., Mozell, M.M., Sheehe, P.R., and Hornung, D.E. (1987). A quantitative analysis of sniffing strategies in rats performing odor detection tasks. Physiol. Behav. *41*, 59–69. https://doi.org/10.1016/0031-9384(87)90131-4.

37. Eiting, T.P., and Wachowiak, M. (2018). Artificial Inhalation Protocol in Adult Mice. Bio. Protoc. *8*, e3024. https://doi.org/10.21769/Bio-Protoc.3024.

38. Mozell, M.M., Sheehe, P.R., Hornung, D.E., Kent, P.F., Youngentob, S.L., and Murphy, S.J. (1987). "Imposed" and "inherent" mucosal activity patterns. Their composite representation of olfactory stimuli. J. Gen. Physiol. *90*, 625–650. https://doi.org/10.1085/jgp.90.5.625.

39. Hahn, I., Scherer, P.W., and Mozell, M.M. (1994). A mass transport model of olfaction. J. Theor. Biol. *167*, 115–128. https://doi.org/10.1006/jtbi.1994.1057.

40. Stringer, C., Pachitariu, M., Steinmetz, N., Reddy, C.B., Carandini, M., and Harris, K.D. (2019). Spontaneous behaviors drive multidimensional, brain-wide activity. Science *364*, eaav7893. https://doi.org/10.1126/science.aav7893.

41. Mimica, B., Tombaz, T., Battistin, C., Fuglstad, J.G., Dunn, B.A., and Whitlock, J.R. (2023). Behavioral decomposition reveals rich encoding structure employed across neocortex in rats. Nat. Commun. *14*, 3947. https://doi.org/10.1038/s41467-023-39520-3.

42. Musall, S., Kaufman, M.T., Juavinett, A.L., Gluf, S., and Churchland, A.K. (2019). Single-trial neural dynamics are dominated by richly varied movements. Nat. Neurosci. *22*, 1677–1686. https://doi.org/10.1038/s41593-019-0502-4.

43. Schneider, D.M. (2020). Reflections of action in sensory cortex. Curr. Opin. Neurobiol. *64*, 53–59. https://doi.org/10.1016/j.conb.2020.02.004.

44. Parker, P.R.L., Brown, M.A., Smear, M.C., and Niell, C.M. (2020). Movement-Related Signals in Sensory Areas: Roles in Natural Behavior. Trends Neurosci. *43*, 581–595. https://doi.org/10.1016/j.tins.2020.05.005.

45. Miura, S.K., and Scanziani, M. (2022). Distinguishing externally from saccade-induced motion in visual cortex. Nature *610*, 135–142. https://doi.org/10.1038/s41586-022-05196-w.

46. Bedell, H.E., Tong, J., and Aydin, M. (2010). The perception of motion smear during eye and head movements. Vis. Res. *50*, 2692–2701. https://doi.org/10.1016/j.visres.2010.09.025.

47. Vélez-Fort, M., Bracey, E.F., Keshavarzi, S., Rousseau, C.V., Cossell, L., Lenzi, S.C., Strom, M., and Margrie, T.W. (2018). A Circuit for Integration of Head- and Visual-Motion Signals in Layer 6 of Mouse Primary Visual Cortex. Neuron *98*, 179–191.e6. https://doi.org/10.1016/j.neuron.2018.02.023.

48. Guitchounts, G., Masís, J., Wolff, S.B.E., and Cox, D. (2020). Encoding of 3D Head Orienting Movements in the Primary Visual Cortex. Neuron *108*, 512–525.e4. https://doi.org/10.1016/j.neuron.2020.07.014.

49. Bouvier, G., Senzai, Y., and Scanziani, M. (2020). Head Movements Control the Activity of Primary Visual Cortex in a Luminance-Dependent Manner. Neuron *108*, 500–511.e5. https://doi.org/10.1016/j.neuron.2020.07.004.

50. Bekkers, J.M., and Suzuki, N. (2013). Neurons and circuits for odor processing in the piriform cortex. Trends Neurosci. *36*, 429–438. https://doi.org/10.1016/j.tins.2013.04.005.

51. Pachitariu, M., Shashwat, S., and Stringer, C. (2023). Solving the spike sorting problem with Kilosort. bioRxiv. https://doi.org/10.1101/2023.01.07.523036.

52. Shamash, P., Carandini, M., Harris, K.D., and Steinmetz, N.A. (2018). A tool for analyzing electrode tracks from slice histology. Preprint at bioRxiv. https://doi.org/10.1101/447995.

53. Claudi, F., Tyson, A.L., Petrucco, L., Margrie, T.W., Portugues, R., and Branco, T. (2021). Visualizing anatomically registered data with brainrender. Elife *10*, e65751. https://doi.org/10.7554/eLife.65751.

54. Harris, C.R., Millman, K.J., van der Walt, S.J., Gommers, R., Virtanen, P., Cournapeau, D., Wieser, E., Taylor, J., Berg, S., Smith, N.J., et al. (2020). Array programming with NumPy. Nature *585*, 357–362. https://doi.org/10.1038/s41586-020-2649-2.

55. Hunter, J.D. (2007). Matplotlib: A 2D Graphics Environment. Comput. Sci. Eng. *9*, 90–95. https://doi.org/10.1109/MCSE.2007.55.

56. Virtanen, P., Gommers, R., Oliphant, T.E., Haberland, M., Reddy, T., Cournapeau, D., Burovski, E., Peterson, P., Weckesser, W., Bright, J., et al. (2020). SciPy 1.0 Contributors. SciPy 1.0: Fundamental Algorithms for Scientific Computing in Python. Nat. Methods *17*, 261–272. https://doi.org/10.1038/s41592-019-0686-2.

57. Pedregosa, F., Varoquaux, G., Gramfort, A., Michel, V., Thirion, B., Grisel, O., Blondel, M., Prettenhofer, P., Weiss, R., and Dubourg, V. (2011). Scikit-learn: Machine learning in Python. J. Mach. Learn. Res. *12*, 2825–2830. https://doi.org/10.5555/1953048.2078195.

58. Meyers, E.M. (2013). The neural decoding toolbox. Front. Neuroinf. *7*, 8. https://doi.org/10.3389/fninf.2013.00008.

STAR★METHODS

KEY RESOURCES TABLE

REAGENT or RESOURCE	SOURCE	IDENTIFIER
Chemicals, peptides, and recombinant proteins		
alpha-pinene	Sigma-Aldrich	Cat#147524; CAS: 80-56-8
eucalyptol	Sigma-Aldrich	Cat#C80601; CAS: 470-82-6
(R)-(+)-limonene	Sigma-Aldrich	Cat#183164; CAS: 5989-27-5
methyl butyrate	Sigma-Aldrich	Cat#246093; CAS: 623-42-7
eugenol	Sigma-Aldrich	Cat#W246719; CAS: 97-53-0
dicyclohexyl disulfide	Sigma-Aldrich	Cat#W344818; CAS: 2550-40-5
methyl 2-furoate	Sigma-Aldrich	Cat#129852; CAS: 611-13-2
p-cymene	Sigma-Aldrich	Cat#C121452; CAS: 99-87-6
Deposited data		
Mouse Brain [brain atlas]	Allen Institute for Brain Science	Available from atlas.brain-map.org
Experimental models: Organisms/strains		
C57BL/6J mice	Jackson Laboratory	RRID: IMSR_JAX:000664
Software and algorithms		
Original code	Iurilli Lab	Zenodo: http://doi.org/10.5281/zenodo.10381293
MATLAB version 2022b	The MathWorks, USA	RRID: SCR_001622; www.mathworks.com
FMAToolbox	Michael Zugaro	RRID: SCR_015533; http://fmatoolbox.sourceforge.net/
KiloSort3	Pachitariu et al., 2023[51]	RRID: SCR_016422; https://github.com/MouseLand/Kilosort
Phy	Cyrille Rossant	https://github.com/cortex-lab/phy
Allen CCF	Shamash et al., 2018[52]	https://github.com/cortex-lab/allenCCF
Brainrender	Claudi et al., 2021[53]	https://github.com/brainglobe/brainrender
glmnet	Qian J., Hastie T., Friedman J., Tibshirani R. and Simon N.	https://hastie.su.domains/glmnet_matlab/index.html
SciPy ecosystem of open-source Python libraries (numpy, matplotlib, scipy, etc.)	Harris et al., 2020[54]; Hunter, 2007[55]; Virtanen et al., 2020[56]	RRID: SCR_008058; https://projects.scipy.org/
Python scikit-learn library	Pedregosa et al., 2011[57]	RRID: SCR_002577; https://scikit-learn.org/stable/index.html
Neural Decoding Toolbox	Meyers, 2013[58]	RRID: SCR_009012; http://www.readout.info/ndt-version-1-0-4-is-released
libsvm	Chang C.C. and Lin C.J.	RRID: SCR_010243; https://www.csie.ntu.edu.tw/~cjlin/libsvm
Other		
Phase 3B Neuropixels 1.0 silicon probes	imec, Belgium	www.neuropixels.org
Flow sensor	Honeywell	AWM3300V
Photo-ionization detector	Aurora Scientific	200B miniPID

RESOURCE AVAILABILITY

Lead contact
Further information and requests for resources should be directed to the lead contact, Giuliano Iurilli (giuliano.iurilli@iit.it).

Materials availability
This study did not generate new unique reagents.

Data and code availability
- All processed data reported in this paper will be shared by the lead contact upon request.

- The code used in the current study is available online. The DOI is listed in the key resources table.
- Any additional information required to reanalyze the data reported in this paper is available from the lead contact upon request.

EXPERIMENTAL MODEL AND STUDY PARTICIPANT DETAILS

Mice

All experimental manipulations were performed according to Italian legislation (DL 26/214, EU 63/2010, Ministero Della Sanità, Roma) and FELASA recommendations for the care and use of laboratory animals. Animal research protocols were reviewed and consented to by the Italian Ministry of Health.

We used 6-9 weeks old C57BL/6J mice of both sexes (Jackson Laboratory, RRID:IMSR_JAX:000664). Mice were co-housed with their littermates (2-4/cage) and maintained on a 12 hr/12 hr light/dark cycle at room temperature (20-22°C), 40-60% humidity, with food and water *ad libitum*. Littermates were randomly assigned to experimental groups. Males and females were randomly assigned. Four C57BL/6 mice were used for the two odors/three concentrations (0.01, 0.1, and 1% v./v.) experiments; two C57BL/6 mice were used for the four odors/two concentrations (0.01 and 0.1% v./v.) experiment; four C57BL/6 mice were used for the odor identity experiments; three C57BL/6 mice were used for the artificial inhalation experiment; four C57BL/6 mice were used for the bulbectomy experiment; five C57BL/6 mice were used for the AEN neurectomy experiment. None of the mice was involved in other procedures. No analysis of the influence of sex on the results of the present study was conducted because it was not relevant to the scope of the study.

METHOD DETAILS

Surgical procedures

Animals were anesthetized with isoflurane (3% induction, 1.5% maintenance) and placed on a custom-made feedback-controlled heating pad. Pre-operative analgesia was induced through intramuscular injection of a bolus (4μl/g) of carprofen (Rimadyl, 0.05%)/dexamethasone (0.01%) and scalp infiltration of a tetracaine solution (0.05%). Post-operative analgesia was provided through carprofen diluted in the water bottle (Rimadyl, 134μl/100ml) following the procedure. Silicone-based eye ointment was applied on the eyes to protect the corneas during the surgery.

Anesthetized mice were mounted in a stereotaxic frame. The scalp was shaved with shaving cream and cleaned with isopropyl alcohol and iodopovidone. The skin and the periosteum from the lambdoid to the frontonasal sutures were removed, and muscles were partially detached from the skull to expose the occipital bone and the parietal ridges. To increase adherence of the implant to the skull, superficial grooves were drilled in the frontal, parietal, interparietal, and occipital bones. After leveling the skull yaw, pitch, and roll to obtain a flat skull configuration, two small reference crosses were scored using a scalpel at bregma and at the entry point of the Neuropixels probe (AP: 2.0/2.1 mm; ML: -2.0/-2.1 mm from bregma), and the incisions were filled with surgical ink and covered with UV-curable acrylic (Optibond). Finally, a titanium headplate was mounted onto the arm of the stereotaxic manipulator and attached to the skull with cyanoacrylate (Loctite 454) and dental cement (Paladur).

Two days before the recording mice were anesthetized again and placed in the stereotaxic manipulator. Two small craniotomies were opened: one for probe insertion (AP: 2.0/2.1 mm; ML: -2.0/-2.1 mm from bregma) and the other over the contralateral posterior parietal cortex for the ground electrode. The dura mater was not removed. Finally, the two craniotomies were filled with surgical silicone (Kwik-Cast, WPI).

To probe PCx responses to the mechanical stimulation of the nasal cavity, we resorted to artificial ventilation. The electrophysiological recordings were performed immediately after the surgical preparation. For this procedure, mice were kept anesthetized throughout the surgical procedure and the recording with urethane (0.9 g/kg). Following a previously developed method[37], we placed a cannula into the nasopharynx via the upper part of the trachea to allow the artificial suction of air through the nasal cavity; another cannula was placed in the lower end of the trachea to allow the natural gas exchange with the lungs.

Somatosensory deafferentation was obtained by sectioning the anterior ethmoidal nerve under isoflurane anesthesia before the recording session. The ocular bulb was laterally retracted, the upper region behind the eye was infiltrated with tetracaine solution (0.05%), and the nerve was cut by blunt dissection with fine forceps at the exit from the ethmoid foramen. The cut was verified post-mortem by visual inspection.

Olfactory deafferentation was obtained by aspirating the OBs using a blunted needle attached to a vacuum system, while Ringer's solution was continuously applied to cleanse the craniotomy site and remove all olfactory nerves down to the cribriform plate. The cavity was then filled with a sterile gelatin sponge (Gelfoam) and sealed with dental cement. Post-mortem verification of bulbectomy completeness was conducted by visually examining coronal brain sections, with any subjects displaying identifiable glomeruli being omitted from further analysis.

Habituation to the experimental rig

Mice were habituated to head-fixation and the experimental rig starting five days before the experiment. Three habituation sessions of increasing duration (20, 40, and 60 min) were run over consecutive days. During the familiarization and the recording sessions, the mouse sat inside a 3-D printed black plastic tube, leaving exposed only the head. A custom-made polyether ether ketone (PEEK)

nose cone was positioned in front of the mouse, loosely fitting the mouse's snout. The nose cone was used to record the breathing signal and deliver the odorants during the experiments.

Stereotaxic probe insertion

All recordings were performed using Neuropixels 1.0 probes. The probe was mounted to a dovetail and affixed to a steel rod held by a micromanipulator (Luigs and Neumann). Before insertion, the back of the probe was coated with a solution of DiI (Thermofisher) using a paintbrush. Next, the silicone plug was removed from the craniotomies, and the probe was positioned above the recording site craniotomy (AP: 2.0/2.1 mm; ML: -2.0/-2.1 mm from bregma). Next, the probe was advanced through the dura and the cortex at approximately 5 μm/s until reaching the PCx (DV: 5.2/5.5 mm from bregma). The exact position depended on identifying a region with high firing rates and breathing-coupled activity. Then, the probe was retracted by 100 μm to allow the brain tissue to settle for 30 minutes before starting the recording. An Ag/AgCl electrode placed over the contralateral posterior parietal cortex was used for grounding. After electrode insertion, craniotomies were covered with a drop of agar solution (1% in Ringer's solution). Neuro-pixels data were acquired and recorded at 30 kHz through a PIXe interface board connected to a PC.

Experimental signals

Four signals were acquired besides the neural data: (1) a breathing signal generated by a flow sensor (AWM3300V Honeywell) plugged into the nose cone; (2) an odor signal generated by a photo-ionization detector (200B miniPID, Aurora Scientific) that sampled the odorant inside the nose cone; (3) a TTL signaling the start of each odor trial and (4) a TTL signal generated by a Bpod Analog Input module (Sanworks) at the start of each inhalation. To identify the onset of an inhalation online, the breathing signal was fed into the Bpod Analog Input module, and a threshold was set at the breathing signal zero-crossing before the inhalation peak. All signals were digitized and recorded at 30 kHz using an Intan RHD2000 board. Finally, to align the neural data with the other signals, a 1 Hz TTL clock signal (50% duty cycle) or a barcode was generated by an Arduino One board and recorded by the PIXe board and the Intan board.

Odor delivery

Odorant stimuli were delivered using 5 seconds of odorant pulses. Odorants were delivered in 8 blocks (trials) for the two odors/three concentrations experiments, 16 blocks for the four odors/two concentrations experiments, and 10 blocks for the ten odors/one concentration experiments. The order of the odorants was randomized within each block. The inter-stimulus interval was randomly drawn from an exponential distribution (mean: 40 s, min-max: 30-50 s).

Odorants were delivered using a custom-made Arduino-controlled 13-valve olfactometer that delivers up to 12 odorants separately. The 13th valve was used to deliver a blank stimulus (no odor) between odor presentations. A vacuum continuously exhausted lingering odors. Odorants were contained in 15 ml vials partially filled with glass beads (Sigma-Aldrich). The headspace and the volume of odorant inside the vial were chosen to ensure that the amount of odor delivered within and across trials was steady as assessed by PID measurements. Each vial was separately connected to an olfactometer valve through a 3 in.-long PTFE tubing. A custom software controlled valve opening and closing, enabling switching between odor vials and a blank vial. At the beginning of a trial, the opening of an odor valve was synchronized with the onset of inhalation, as detected by the Bpod Analog Input Module.

Two streams of carbon-filtered air (F1 and F2) were independently routed to the nose cone at 1 l/min. The F1 stream consisted in odor (F1O; 0.1 l/min) and carrier (F1C; 0.9 l/min) streams mixed. Upon opening an odorant valve, the F1O flow was routed through the open vial to a PEEK manifold using a 3 in.-long PTFE tubing. Inside the manifold, the F1O flow from the open vial was mixed with the F1C flow to obtain the F1 airflow. The outlet of the mixing manifold was connected through a 0.5-in.-long PTFE tubing to a final three-way valve (V1). The F2 stream was directly connected to a second three-way solenoid valve (V2). The V1 and V2 valve outlets converged in a final 0.5 in. PTFE tubing connected to the nose cone. The F1 and F2 airflows reached the odor cone during odor-ON and odor-OFF epochs, respectively. The V1 outlet was open during the odor-ON epoch, whereas the V2 outlet was open during the odor-OFF epoch. At the beginning of a trial, the olfactometer opened the odor vial valve to load the tubing with odorized air up to the final valve V1, which diverted the flow outside the nose cone. After 2 seconds, the onset of an inhalation triggered an "odor-ON" TTL that switched the outlet opening of the V1 and V2 valves such that only the odorized airflow F1 entered the nose cone. After 5 seconds from the odor-ON TTL, the odor vial valve closed. After 10 seconds from the closing of the odorant vial valve, the V1 and V2 valves were switched to the odor-OFF configuration.

The olfactometer was calibrated to generate the final odor concentration within ~ 200 ms from the opening of the final valve (Figure S6C). No attempt was made to remove a small pressure transient at the opening of the final valve.

The odor panel included two odors (alpha-pinene and eucalyptol) delivered at three concentrations (0.01, 0.1, and 1% v./v.), three odors (limonene, p-cymene, and methyl butyrate) delivered at two concentrations (0.01 and 1% v./v.) and four odors (eugenol, dicyclohexyl disulfide, *p*-cymene, and methyl 2-furoate) delivered at a single concentration (0.01%). All odors were purchased from Sigma-Aldrich. To determine the dilution of each odor, a calibration curve was generated. To this aim, the signal generated by a photo-ionization detector (200B miniPID, Aurora) upon delivery of an odor at three dilutions (no dilution, 1:8, and 1:160 in mineral oil, Sigma-Aldrich; 10 presentations per dilution) was recorded. Then, an exponential curve was fitted to the miniPID traces to obtain the coefficient A for each dilution. Next, a second-order polynomial was fitted to the three A coefficients of each odor. Finally, the

dilutions corresponding to 0.1%, 1%, and 10% v./v. of undiluted odor were extrapolated from the fitted polynomial. The carrier airflow further diluted the odor concentration by 10 to reach the final concentration of 0,01, 0.1, and 1 % v./v.

Artificial mechanical stimulation

The cannula in the nasopharynx was attached to a computer-controlled solenoid valve, which was connected to a vacuum line. The opening of the valve drew air inside the nasal cavity. The air was deodorized through a carbon filter before entering the nose cone. We applied 150-ms pulses of suction at 750-ms intervals. We tested five flow rates that span the range of estimated nasal flow rates in mice (50, 100, 150, 200, and 250 ml/min).

Histology

Mice were deeply anesthetized with 1 g/kg urethane injection and intracardially perfused with 1% phosphate buffer solution (PBS) followed by 4% paraformaldehyde (PFA). The brain was dissected and immersed in 4% PFA for 24 h. Following fixation, the brain was washed with PBS and sectioned coronally (80 μm) with a vibratome. Sections were counter-stained with DAPI, and images were acquired with a fluorescence microscope at 10x magnification. The Allen CCF open-source toolbox[52] was used to reconstruct the probe location in 3D, and Brainrender[53] was used to visualize the probe position.

Experimental design

No statistical methods were used to determine sample sizes. Sample sizes were chosen based on previous publications in the field. Multiple independent samples were collected for each experiment. The number of samples is indicated in the paper. Data collection and analyses were not performed blind to the experimental conditions. The inclusion and exclusion criteria for any data and subjects and the statistical methods are indicated in the Quantification and Statistical Analysis section.

QUANTIFICATION AND STATISTICAL ANALYSIS

Analysis of the breathing signal

The breathing signal was bandpass filtered between 0.5 to 50Hz using the MATLAB FMAToolbox (http://fmatoolbox.sourceforge.net/) and smoothed with a Gaussian kernel (standard deviation: 25 ms). Inhalation peaks were identified as the local minima of the respiratory signal. Inhalation peaks closer than 65 ms from the next peak were discarded. Inhalation onset and offset were identified as the breathing signal zero-crossings before and after the inhalation peak. Inhalation length was defined as the difference between the inhalation offset and onset times. The breathing cycle was calculated as the difference between two consecutive inhalation onsets. The negative inhalation slope was defined as the slope of the line between the nearest two points before the inhalation peak in the z-scored respiration signal with a value equal to 10% and 90% of the inhalation peak amplitude. Similarly, the positive inhalation slope was calculated as the slope of the line between the 90% to 10% of inhalation amplitude points in the z-scored respiration signal after the inhalation peak.

Inhalation clustering

Inhalation waveforms were isolated by extracting the breathing signal within a 100 ms-long window centered on the inhalation peak. Each waveform was normalized by its 2-norm and considered as a point in a high-dimensional space. The dimensionality of the inhalation space was reduced by applying PCA using the *'pca'* function in MATLAB (Mathworks®). The projection of the inhalation vector onto the *n*-dimensional subspace spanned by the *n* first PCs (where *n* is the minimum number of PCs that explain at least 98% of total variance) was calculated. The first PC captured most of the dynamics of an inhalation (Figure S6A). The inhalation vectors in the *n*-dimensional space were clustered with a Gaussian Mixture Model using the *'fitgmdist'* function in MATLAB (maximum number of iterations: 10,000, regularization value: 0.05, replicates: 15, full covariance matrix). The Calinski-Harabasz index was used to determine the optimal number of clusters. The centroid vector for each cluster was defined as the mean vector of all inhalation vectors within the cluster. To consolidate the GMM clustering, a Hierarchical Cluster (HC) dendrogram was applied to the centroid vectors using the *'linkage'* function in MATLAB (distance metric: correlation). The HC dendrogram from an individual experiment usually resulted in two or three clusters. Visual inspection of the dendrograms suggested that two clusters were similar and stemmed from the same branch; thus, we merged the two clusters with the same parent. Finally, we assigned the clusters to the "slow" and "fast" inhalation types based on the mean of the inhalation lengths within each cluster, with "fast" inhalation assigned to the class with smaller inhalation lengths. The clustering algorithm was cross-validated on the inhalations from eight mice by fitting the GMM on a training set consisting of all the inhalations from seven mice and then using the fitted model to predict the labels of the inhalations from the held-out mouse. The ground-truth inhalation labels for the held-out mouse were obtained using the above clustering pipeline. This process was repeated for all possible combinations of test and train sets, and the classification accuracies were finally averaged. This clustering pipeline classified the inhalation label of held-out inhalations with 98% accuracy. The proportion of fast and slow inhalations is reported in Figure S6B.

Spike sorting and inclusion criteria

Spike waveforms were sorted using KiloSort3. All clusters were manually curated using Phy (https://github.com/cortex-lab/phy). The clusters were evaluated by examining their firing rate stability during the recording session, the median amplitude of the spike (>50 μV), the auto-correlograms, and the cross-correlograms. The quality of the clusters included in the analyses was further

evaluated by computing the inter-spike-interval (ISI) violation rate (threshold: <0.5; median: 0.01, Q1: 0, Q3: 0.04), the amplitude cut-off (median: 0.0005, Q1: 0.0001, Q3: 0.0015), and the presence ratio (median: 1, Q1: 1, Q3: 1; see also Figures S6D–S6F). Single units with a firing rate of less than 0.5 Hz were excluded from the subsequent analyses; this threshold was lowered to 0.1 Hz in the experiments with tracheostomized mice because the urethane anesthesia reduced the baseline firing rate. Restricting the analyses to only those units with an ISI violation rate < 0.02 gave similar results.

Single units were further classified as regular (RS) or fast-spiking (FS). A weighted average of the contributing cluster templates was computed for each unit, obtaining an average template waveform. Next, three features were extracted:

(1) The latency between the negative and the following (post-depolarization) positive peak of the average waveform;
(2) The asymmetry between the pre-depolarization (p1) and the post-depolarization (p2) peaks of the average waveform, computed as

$$\frac{p2 - p1}{p2 + p1}$$

(3) The average firing rate of the unit across the whole recording.

Finally, a k-means clustering (with Squared Euclidean distance, 10,000 iterations, and 2,500 replicates) of the features was used to partition the units recorded from each mouse into two categories. Units labeled as 'RS' had, on average, lower firing rates, larger trough-to-peak latency, and smaller asymmetry compared to units labeled as 'FS'.

The through-to-peak latency and the asymmetry index were also used to assess the homogeneity of cell-type sampling across the experimental conditions. To this aim, we compared the distributions of the waveform features across all experimental conditions (Figure S6G). Furthermore, a cross-validated Naive Bayes decoder and a linear support vector machine using these waveform features were used to ascertain that the experimental condition could not be decoded from the spike waveforms of the units recorded during that specific condition (Figure S6H).

Analysis of sniff-by-sniff responses

Inhalation and odor response were measured as the average spike count within a 70 or 180 ms window after the inhalation onset. Smoothed peri-event time histograms (PETH) were obtained by convolving the spike-times series within an inhalation with a Gaussian kernel (standard deviation: 10 ms), then averaging across all inhalations of the same type and finally subtracting the average firing rate across the odor-free epochs of the entire recording session. PETHs were aligned at the inhalation onset. Odorless-air inhalations were defined as those occurring within the -13 to -4 seconds window before the delivery of an odor. This window was considered sufficient to remove any lingering odor because the minimum time interval between two odor presentations was 30 seconds, and a vacuum line constantly exhausted odorants from the nose mask. Sniff-by-sniff odor responses were measured in a time window starting at the odor onset and lasting for 5 seconds. The first two trials of each odor-concentration stimulus were excluded to avoid any bias due to the novelty of the stimulus.

To ascertain whether a neuron responded to an inhalation, the spikes within a window comprising the inhalation onset (from -300 to + 400 ms) were binned using an adaptive binning method, guaranteeing at least five spikes per bin. Then, the spike counts in those bins were compared against those generated by a homogenous Poisson process using a chi-square test. The constant rate of the homogenous Poisson process was set to the mean firing rate of the recorded neuron. Responses to first sniffs were tested by comparing the spike counts in a 180 ms window post-inhalation onset in the first sniff after at least five consecutive slow inhalations against the spike counts in a 180 ms window post-inhalation onset in the remaining slow inhalations. For all these analyses, only odorless inhalations were considered.

Concentration discrimination index

To measure how well a neuron could discriminate two concentrations, we first computed an area-under-the-receiver-operating-curve (auROC) using the spike counts during the inhalation of 0.01 and 0.1% v./v. odorant. The CDI was computed as abs(1 - 2*auROC). To generate the spike count distribution for each concentration, a random sample of inhalations was taken during the presentation of that concentration; an equal sample size was used for the two concentrations. Next, three different CDI were calculated based on a sample of slow inhalations, fast inhalations, and mixed slow and fast inhalations; 100 samples were drawn for each set of inhalations, and an average CDI was calculated for slow, fast, and mixed inhalations.

Tuning curves

To obtain neural tuning curves during artificial stimulation of the nasal cavity, the average response for each airflow rate was calculated as the difference between the number of spikes fired by a neuron during the (0 500] and (-500 0] ms window where 0 is the onset of the air pulse.

To obtain neural tuning curves during natural breathing, inhalations were sorted into ten quantile bins based on the amplitude of the peak of airflow as measured by the flow sensor. This was done to ensure that each bin contained an equal number of inhalations. The tuning curve was generated by using the average response to an odorless inhalation during the first 180 ms for each bin.

Tuning curves were z-scored, and their slopes were calculated by linearly regressing the neural response to the airflow rate.

Encoding models

A Poisson Generalized linear model (GLM) with regularization was employed to estimate the contribution of inhalation speed, odor concentration, and their interaction with the sniff-by-sniff odor response of a neuron. The model aimed to predict the spike count (y_i) of neuron i during a single inhalation (either first 180 ms or 70 ms) using the following equation:

$$y_i \sim \text{Poiss}\left(\exp(\alpha_i I + \beta_i C + \gamma_i IC + y_{0i})\right)$$

Here, the I term represents the inhalation speed (0 for slow and 1 for fast), and the C term represents the odor concentration (logarithm of the three concentrations 0.01, 0.1 and 1% v./v.). y_{0i} is a baseline bias of the response. The GLM was fitted using the *glmnet* toolbox (https://hastie.su.domains/glmnet_matlab/) in MATLAB (Mathworks®) with elastic net regularization, where the parameter *alpha* controlled elastic net penalty. A value of 0.95 was used for *alpha*, which smoothly interpolates the gap between lasso (*alpha* = 0) and ridge regression (*alpha* = 1). The optimal elastic net penalty value was selected using a 10-fold cross-validation approach.

We used a linear regression model for the simulations shown in Figures 5E–5I and Figures 6B and 6C. In this case, the normalized firing rate r_i of neuron i during the first 180 ms of inhalation was modeled with the following equation:

$$z\ score\ (r_i)\ =\ \alpha_i I + \beta_i C + r_{0i} + \eta$$

Here, the I term represents the inhalation speed (0 for slow and 1 for fast), and the C term represents the odor concentration (varying from 0 to 1 based on the logarithm of the concentration). The term r_0 is a baseline bias, and η is a Gaussian noise term. To fit the models, inhalations were randomly sampled from all inhalations to have an equal size for each combination of inhalation speed and odor concentration term. The vector of the neural responses to the inhalations was z-scored and passed to the model with the corresponding design matrix. The significance of the model's coefficients was assessed using an ANOVA test. The random sampling was repeated 100 times, and the coefficients of each term and their p-values were averaged across all re-samplings.

Prediction of encoding properties from waveforms

To assess if the encoding differences we detected across cells could be linked to cell type differences, we searched for statistical dependencies between the α and β parameters and the spike waveform shape on a cell-by-cell basis. We built and tested predictive models that attempted to predict the values of α, β and α and β jointly from the asymmetry index and the through-to-peak depth of the waveforms (this analysis was conducted with *scikit-learn*). We considered three different models, each of which is well suited to capture very different types of patterns in data: a linear model with elastic-net regularization (95% ridge, 5% lasso), a K-nearest-neighbor (KNN) regressor, and a set of bagged trees. We tested each model with 10-fold cross-validation (CV; with folds taken over the set of cells). The shrinkage hyperparameter of the GLM was selected by nested 10-fold cross-validation, meaning that for each training fold in the outer CV loop, the value of the hyperparameter was selected by cross-validation on the training data only. The number of neighbors to use in KNN was selected the same way. The set of bagged trees comprised 1000 decision trees, each grown on a bootstrap replicate of the training data. The trees were grown until no splits could be performed without resulting in at least one leaf containing fewer than 5 data points. We standardized the data before training the predictive models. We tested the performance of the models separately at predicting α, predicting β, and predicting α and β jointly. This resulted in 3 models x 3 tests = 9 assessments. In none of the 9 cases, the predictive model could extract a significant relationship (as measured by the cross-validated R^2 of the regression) between the spike waveform and the encoding parameters.

Pseudo-population response matrix

The pseudo-population response matrix was obtained by pooling all recorded neurons' sniff-by-sniff spike count responses to the inhalation events from all animals within the same experimental design. To create this matrix, an equal number of inhalation events for each odor concentration were randomly drawn from all inhalation events of all mice. Half of these events were fast inhalations, and the other half were slow inhalations. This allowed for an equal representation of both inhalation types in the sample. The same number of inhalations was sampled for each concentration, and then all inhalations were pooled. The response of each neuron to each inhalation in the selected sample was then vertically concatenated to obtain a population response vector during an inhalation. Finally, the response vectors of all neurons were concatenated horizontally to create a pseudo-population response matrix.

PCA embeddings

To visualize the neural representation of odor concentrations across different inhalation speeds, PCA analysis was performed on the response covariance matrices obtained from a neural pseudo-population or single mouse neural populations. Before applying PCA, the neural responses of individual neurons were z-scored. PCA was also used to determine the projections onto the first 15 PCs of the

sniff-by-sniff responses; these projections were separately used to decode inhalation speed in Figure 5B and Figures S5B and S5D and odor concentration and identity in Figures 5B–5D and Figures S5B, and S5D–S5F.

Angle between encoding axes

The encoding direction for odor concentrations and inhalation speed was determined using concentration-encoding unit vectors and sampling-encoding unit vectors; these two vectors were defined as unit vectors in the sniff-by-sniff response space. Linear discriminant analysis (LDA) was used to calculate the encoding vectors. Specifically, a pseudo-population response matrix with corresponding labels for each odor concentration and inhalation speed was used to fit the LDA model. This operation was performed using the Python *scikit-learn* library[57]. The eigenvalue decomposition solver was used to fit the LDA model with a shrinkage parameter that was automatically calculated by the Ledoit-Wolf lemma algorithm. The encoding vector was taken as the first column of the LDA transform scaling matrix. For each inhalation speed, the concentration-encoding unit vector was obtained from the LDA fit by using a pseudo-population response during a given inhalation speed and concentration using a different label for each concentration. Similarly, the inhalation-encoding unit vector was obtained from the LDA fit using pseudo-population response during either inhalation speed, and the type of inhalation speed was used as a label. Finally, the average angle between the concentration-encoding vectors for each inhalation speed and the average angle Θ between the concentration-encoding vectors and inhalation-encoding vectors were calculated and then transformed as: $\Theta' = 90 - |90 - \Theta|$. This procedure was repeated 100 times with pseudo-population response matrices built using different randomly sampled neurons for each run.

Inhalation speed decoding

A linear support vector machine (lSVM) classifier was utilized for all classification analyses (inhalation speed, odor concentration, odor identity, and generalization analysis). The lSVM was implemented using the MATLAB (Mathworks®) Neural Decoding Toolbox (NDT)[58] and *libsvm* (http://www.csie.ntu.edu.tw/%7Ecjlin/libsvm/) toolbox. A 10-fold cross-validation was performed for all models. Before model fitting, the sniff-by-sniff neural responses in the training and test set were normalized by subtracting the means and standard deviations calculated from the responses in the training set.

To decode the inhalation speed, a pseudo-population response matrix was generated using only the spike counts during 180 ms windows for each inhalation of odorless air. Specifically, 400 random slow and fast inhalations were drawn, and the spike counts in 180 ms windows were used to build the response matrix of a pseudo-population or an individual mouse population. The decoding accuracy for different numbers of neurons was determined by drawing random subsamples of neurons of different numerosity. This resampling process was repeated 100 times for each number of neurons to obtain reliable estimates of decoding accuracy. Additionally, the entire classification process was repeated 100 times, randomizing the sampled inhalation events included in each run. The reported accuracy for each number of neurons represents the mean of all resampling processes.

Concentration decoding

To classify odor concentration (0.01, 0.1, and 1% v./v.), a pseudo-population response matrix or a single animal population response matrix was built using the same number of inhalations for each odor-concentration pair to avoid any potential bias due to different inhalation sample sizes. Next, for each odor, corresponding rows of this matrix or its PC projections were sorted and passed to the classifier to decode the concentration in either the whole population response space or its PC projections space. This procedure was repeated 100 times with pseudo-population response matrices with different randomly sampled inhalations. The reported accuracies are the mean and standard deviation across all resampling processes.

To investigate the geometry of the neural space, a generalization paradigm was employed. To this end, a lSVM trained on data from one inhalation speed was tested on data from the other inhalation speed (*trans*-decoder). The average accuracy of *trans*-decoders was compared to that of *cis*-decoders that had been trained and tested instead on the odor responses during the same inhalation speed.

To assess the importance of heterogeneous selectivity for mechanosensory and olfactory inputs for sniff-invariant odor representations, we first fit the sniff-by-sniff responses of individual neurons with a linear regression model including a concentration (C = 0.01, 0.1, and 1%) and an inhalation speed (slow: I = 0; fast: I = 1) regressor. Then we selected a sub-pseudo-population with highly correlated mechanosensory (α) and olfactory regressor coefficients (β). To this end, a sub-pseudo-population of neurons meeting the following conditions were considered positively correlated: ($|\beta| \geq |\alpha*\tan(pi/12)|$) and ($|\beta| \leq |\alpha*\tan(5*pi/12)|$) with α and β having the same sign. Finally, another subset of neurons with α and β having different signs was selected to build a sub-pseudo-population with negatively correlated mechanosensory and concentration regressors. The union of these two sets was considered as the uncorrelated sub-pseudo-population. Then, an equal number of neurons was randomly sampled from these three sub-pseudo-populations, and their sniff-by-sniff odor responses were used by *cis*- and *trans*-decoders.

To decode odor concentration over time and phase bins, we used the following procedure:

Feature vectors generation

First, we generated time- and phase-binned vectors of neuronal activity after the inhalation onset as follows:

(1) Time-binned vectors of 180 ms: the firing rate traces of all neurons in an area were used, as defined in the above section *Decoding of the inhalation phase. Preprocessing.* The traces were cropped from the onset of each inhalation in a 180 ms

window and binned in 10-ms bins. Then, the traces of all neurons were concatenated to obtain, for every inhalation, an array with size (n_timebins x n_neurons), with n_timebins = 18.

(2) One-bin time vectors: the time-binned arrays defined above were averaged over the time bins.

(3) Time-binned vectors cropped over a full inhalation cycle: the respiratory phase was computed using the Hilbert transform. The time window in which the respiratory phase increased by 2π was found for every inhalation. Then, the firing rate trace was cropped in this window, padding it with zeros to account for the different durations of each inhalation period to a total of 500 ms (enough to accommodate > 99% of all inhalations). The arrays were then binned in 10-ms bins and concatenated across neurons to a total of (n_timebins x n_neurons) for every inhalation, with n_timebins = 50.

(4) Phase-binned vectors: the respiratory phase was computed using the Hilbert transform. The time window in which the respiratory phase increased by 2π was found for every inhalation. The firing rate trace was cropped in this window and then binned into 36 bins equally spaced in phase (in this case, no zero-padding was necessary). Next, the activity of all neurons was concatenated to obtain an array with length (n_phasebins x n_neurons) for every inhalation, with n_phasebins = 36 and zero-padding at the end to ensure array length consistency.

Odor concentration decoding

To decode odor concentration from the firing rates, we used an SVM classifier using a generalization procedure like the one described above. First, inhalations were sampled 100 times with replacement for every animal to obtain a consistent number of events for each combination (inhalation_type, concentration). Then, ten-fold validation was used for training and testing the classifier for each extraction. Data were split into ten blocks, and the SVM trained over nine blocks and tested over the remaining one iterating over all ten possible left-out blocks. The SVM model was trained using SVC from sklearn.svm, and its default parameters but for the linearity of the kernel (kernel = linear, gamma = 'scale', coef0 = 0.0, tol = 0.001, C = 1.0, epsilon = 0.1, shrinking = True; where 'scale' gamma is 1/(n_features * X.var())). The source data was the ((n_bins x n_neurons), n_inhalations) array of concatenated firing rates over time for each inhalation; the variable to predict was the (n_inhalations) array of concentrations presented during each inhalation. For each iteration, the SVM was evaluated by computing the fraction of correct predictions. This number was then averaged across all folds and samplings (1000 different classifications) to obtain the numbers reported in the figures. Finally, the analysis was repeated separately for the two presented odors, and the results eventually merged.

Inhalation phase decoding

To predict the inhalation phase from neuronal activity, we employed Support Vector Regression (SVR) using the *scikit-learn* library[57].

Preprocessing

First, the firing rate for every neuron was computed using a rolling gaussian window with sd = 20 ms (gaussian_filter() from scipy.ndimage). The firing rate matrix and the respiration trace were then downsampled to 10 ms bins to speed up the following computations. For every animal, the analysis was restricted to areas with at least 20 recorded neurons.

Inhalation phase

Analysis was restricted to the inhalation events defined and classified as described in the section *Inhalation clustering*. The inhalation phase was a number in the interval [0, 1] where 0 and 1 corresponded to the beginning and the end of the inhalation event, and the other values were linearly interpolated.

PCA decomposition

First, neuronal activity from all the neurons of each area was projected over principal components using the PCA class from sklearn.decomposition. To focus on the most relevant components for the prediction, PCs up to a cumulative explained (relative) variance > 0.5 were included (at least two PCs were always selected). We note that the analysis results hold for different inclusion criteria for the number of PCs.

Epochs definition

For the training and testing of the model, suitable non-overlapping epochs were created by concatenating inhalation periods for a total duration of 30 s. Depending on the inhalation number and classification, this resulted in a variable number of epochs (between 2 and 4) for every experimental animal. For every animal, all permutations of pairs of those suitable epochs were used as test and training datasets. Results were robust to different choices of epochs (i.e., more epochs with shorter windows).

SVR training

An SVR model was trained using SVR from sklearn.svm(), and its default parameters (kernel = 'rbf', degree = 3, gamma = 'scale', coef0 = 0.0, tol = 0.001, C = 1.0, epsilon = 0.1, shrinking = True; where 'rbf' kernel is the Radial Basis Function, and 'scale' gamma is 1 / (n_features * X.var())). The source data was the (n_components, timepoints) array of PC data; the variable to predict was the (timepoints,) array of inhalation phase data. The shuffle distributions were calculated by randomizing the inhalation phase array before prediction.

Evaluation

For every permutation of the epochs, the inhalation phase was predicted at every time point, and the performance of the model was assessed by calculating the squared Pearson correlation between the ground truth and the predicted data and then averaged across permutations.

Simulation of sniff-induced concentration changes

We tested whether integrating odor-independent mechanosensory inputs in the PCx code offsets the odor concentration alteration (ΔIC) inside the nasal cavity due to changes in inhalation speed. To this end, we compared odor concentration decoding using the activity pattern of two simulated populations of neurons with or without mechanosensory inputs. We reasoned that the ΔIC should be proportional to the external concentration and additive. Thus, we simulated the sniff-by-sniff responses of each neuron using the following Poisson model:

$$R_j = Poiss\left(a_j \, I + \beta_j \, C_n\right), with \; C_n = \log(C_e + k \, I \, C_e)$$

R_j is the simulated neural response during a sniff. a_j and β_j are the mechanosensory and olfactory regressor coefficients previously estimated using a linear regression model fitted to the actual responses of neuron j. I is equal to 0 for slow inhalations and 1 for fast inhalations. C_e is the external odor concentration (0.01, 0.1, and 1%). k is a proportional factor that was parametrically changed in the range between 0 and 1 to simulate different levels of ΔIC; k = 0 means that a slow-to-fast change in inhalation speed does not change the odorant concentration (ΔIC = 0), whereas k = 1 means that a slow-to-fast change in inhalation speed increases the odor concentration inside the naris by 100% of the external concentration (ΔIC = C_e). The population of neurons without mechanosensory inputs was generated by setting α to 0. α was set to 0 to simulate the population of neurons without mechanosensory inputs.

Geometrical proof

Heterogeneous mixed selectivity of neural responses has an immediate connection with the orthogonality of population representations. This can be seen in a simple model, as follows. Consider a population code where the firing rate r_i of cell i is

$$r_i = r_0 + \alpha_i \, I + \beta_i \, C + \gamma_i \, I \, C$$

where, as above, I is the inhalation speed, and C is the concentration. For a population of size N ($1 \leq i \leq N$), we can also write this in vector form as

$$r = r + \alpha \, I + \beta \, C + \gamma \, I \, C$$

where r, α, β, and γ are now vectors with N entries. Assume that the number N of neurons is large and that coding is heterogeneous (that is, there is no special structure to the code), so that α, β, and γ are random vectors in N dimensions. In this case, α can be thought of as a scalar $|\alpha|$ controlling the overall intensity of tuning for inhalation speed in the population, times a random vector on the unit sphere, and the same for β and γ. The direction along which the population vector r encodes the concentration is

$$\frac{dr}{dC} = \beta + \gamma \, I$$

In other words, the concentration C is encoded in the direction β for slow inhalation (I=0) and the direction $\beta + \gamma$ for fast inhalation (I=1). The cosine of the angle θ between the two encoding directions is

$$\cos(\theta) = \frac{<\beta, \beta+\gamma>}{|\beta| \cdot |\beta+\gamma|} = \frac{|\beta|^2 + <\beta, \gamma>}{|\beta|\sqrt{|\beta|^2+|\gamma|^2+2<\beta,\gamma>}}$$

However, if β and γ are high-dimensional and their direction is chosen at random, it can be assumed they are approximately orthogonal, and $<\beta,\gamma> \approx 0$. Accordingly,

$$\cos(\theta) \approx \frac{|\beta|^2}{|\beta|\sqrt{|\beta|^2+|\gamma|^2}} = \frac{|\beta|}{\sqrt{|\beta|^2+|\gamma|^2}}$$

Therefore, the concentration encoding directions will tend towards orthogonality in the presence of strong interactions (when $\gamma >> \beta$, $\cos(\theta)$=0) and will be parallel when interactions are absent or weak (when $|\gamma|$=0, $\cos(\theta)$=1).

Statistical tests

Sample sizes were not estimated in advance. Data groups were tested for normality using Kolmogorov-Smirnov test and then compared using the appropriate test. For regression modeling, confidence intervals were computed over bootstraps (with replacement) of the data. Statistical tests used, the value of n, and what n represents in each analysis can be found in the corresponding figure legend.